aerospace

MDPI

Article

Study on the Flow Mixing and Oblique-Detonation Ignition Characteristics of RP-3 Aviation Kerosene in a Constrained Supersonic Flow Channel

Zijie Wu, Baoxing Li *, Kun Wang, Ronggang Wei, Chengfeng Wu and Shaoqing Hu

Xi'an Modern Chemistry Research Institute, Xi'an 710065, China; 13782747731@163.com (Z.W.); wkxjtu@126.com (K.W.); weironggang0227@mail.nwpu.edu.cn (R.W.); wuchengfeng@tju.edu.cn (C.W.); hsq18191589536@163.com (S.H.)

* Correspondence: lbxnjust@126.com

Abstract

Oblique detonation engines have been proposed for hypersonic propulsion because detonation-based heat addition can, in principle, provide rapid energy release with reduced total-pressure penalties. We investigate non-premixed injection/mixing of an RP-3 aviation-kerosene surrogate in a constrained supersonic channel and its impact on oblique-detonation initiation, stabilization, and static pressure gain. Numerical simulations are performed for a Mach 8 inflow representative of a 30 km altitude condition using an OpenFOAM v7-based reacting-flow solver. We analyze the pressure-gain process following detonation onset, quantify the effects of the inducer-ramp angle, and qualitatively assess the predicted initiation/stabilization trends against direct-connect hot-fire experiments. The results show that non-premixed injection into a supersonic crossflow yields limited mixing over the available mixing length and results in a strongly stratified inflow to the combustor. In the constrained passage, a train of reflected shocks forms and progressively reduces the total-pressure recovery factor along the mixing section, which asymptotically approaches ~0.49. In the combustor, the inducer-ramp angle controls whether and how a stabilized oblique detonation can be established. For a 25° ramp, no self-sustained ODW is obtained under the present conditions, whereas stabilized ODWs are observed for 30° and 35° ramps, exhibiting abrupt and smooth topologies, respectively. These initiation thresholds and stabilized morphologies show qualitative consistency with the direct-connect observations. Due to fuel stratification, pressure gain varies among streamlines but consistently follows a "primary compression–plateau–secondary pressure rise" sequence; the secondary stage contributes approximately 17.54–27.98% of the static pressure rise.

Keywords: constrained channel; RP-3 aviation kerosene; non-premixed mixing; oblique detonation wave; initiation and stabilization

Academic Editor: James 'Chris' Thomas

Received: 8 April 2026
Revised: 19 May 2026
Accepted: 22 May 2026
Published: 23 May 2026

1. Introduction

Driven by mission requirements such as long-range rapid strike and space access/return, hypersonic vehicles demand propulsion systems that combine high specific impulse with compact integration and robust operability under severe thermal constraints. In structurally constrained scramjet configurations, combustion organization is limited by millisecond-scale residence times and strong compressibility associated with intense compression; consequently, fuel–air mixing, ignition, and flameholding often become the primary performance bottlenecks. Although scramjet technology has advanced through

systematic research and engineering demonstrations, significant challenges in combustion efficiency and total-pressure loss remain pronounced under hypersonic conditions [1–5]. In contrast, an oblique-detonation engine (ODE) releases chemical energy through detonation-like heat addition that can approach constant-volume heating in the ideal limit, offering the potential for rapid heat release and static pressure-gain combustion at high Mach numbers [4–6].

For a supersonic inflow, an ODE employs a ramp-induced oblique shock to compress and preheat the combustible mixture prior to onset. When the compression-induced reduction in the chemical induction time becomes comparable to the convective time scale and the required normal detonation speed matches the normal component of the incoming flow velocity, a self-consistent balance among compression, heat release, and wave propagation can be established, yielding a stabilized oblique detonation wave (ODW). This stabilized mode enables energy release over a shorter combustor length while maintaining high thermal efficiency [7–9]. Compared with intrinsically unsteady devices such as pulsed detonation engines and rotating detonation engines, a spatially stabilized ODW front is attractive for integrated inlet–combustor–nozzle layouts [10]. Meanwhile, ODW initiation and stabilization are sensitive to inflow Mach number, equivalence ratio, geometric compression strength, and disturbances; achieving a wide operating range with robust stabilization remains challenging, particularly at engineering scales and under complex boundary conditions [11–14]. Accordingly, the literature has evolved from premixed inflow studies toward increasingly complex inflows, practical fuels, and engineering-relevant confinement effects [9–14].

Recent ODE/ODW studies have further strengthened this engineering-oriented trend. Experimentally, stabilized ODWs have been demonstrated in hypersonic combustible flows, confirming the feasibility of maintaining a stationary detonation front over a ramp under laboratory conditions [15]. For hydrocarbon-fueled ODEs, recent kerosene and RP-3 aviation-kerosene experiments have shown that practical fuels introduce additional difficulties associated with delayed ignition, incomplete vaporization/mixing, and stronger sensitivity to local flow modulation [16]. In parallel, numerical studies on finite-wedge-induced ODWs, expansion-wave-assisted initiation, Mach-reflection destabilization, and jet–wedge combined initiation have indicated that ODW formation in realistic geometries is not governed solely by the nominal inflow Mach number and ramp angle [17–20]. Instead, finite-length effects, confinement-induced reflections, local shock interactions, and fuel–air non-uniformity can jointly alter the initiation pathway, anchoring position, and stabilized wave morphology. These recent advances suggest that practical ODE combustors should be analyzed as coupled mixing–compression–induction–detonation systems rather than as idealized premixed wedge flows.

Under premixed conditions, attention has primarily focused on initiation modes, surface instabilities, and responses to inflow perturbations. Yang investigated ramp-induced ODW evolution under continuous unsteady inflow disturbances, showing that variations in disturbance wavenumber can drive response regimes ranging from quasi-steady behavior to overshoot oscillations and ultimately destabilization, thereby providing a quantitative basis for disturbance tolerance [9]. Teng et al. proposed a transition criterion based on the difference between the oblique-shock angle and the detonation angle, clarified the predictability of different initiation-transition modes, and emphasized that Mach number, heat release, and induction characteristics jointly shape the initiation structure [13]. Their subsequent work provided a systematic analysis of premixed hydrogen–air ODW morphologies, highlighting the link between the wave-system composition in the initiation region and the global stabilized configuration [14]. Teng also conducted a parametric investigation of ramp-induced premixed hydrogen–air ODW, establishing trends with inlet pressure and

Mach number for the initiation structure and initiation length [21]. Yang further examined the influence of inflow Mach number on the initiation structure and the critical Mach number and reported that the heat-release rate can significantly alter the initiation criterion and transition pathway [22]. Collectively, these studies suggest that, for premixed inflows, an ODW can be viewed as a coupled system of "flow compression–chemical induction–detonation formation," where stabilization hinges on matching wave-system compression strength to the induction time scale within the initiation region.

In practical non-premixed operation, fuel is typically injected into a supersonic crossflow and only partially mixes over the available mixing length, yielding a stratified combustor inflow with strong equivalence-ratio gradients. Against this backdrop, several studies have focused on how inlet non-uniformity reshapes oblique detonation wave (ODW) initiation and wave-front topology. Guo et al. showed that imposed equivalence-ratio gradients alter local induction characteristics and wave-front structure, thereby modifying the initiation pathway and the stability window [23]. Using n-dodecane as a kerosene surrogate, Liu et al. further compared uniform and non-uniform mixing conditions and linked mixing inhomogeneity to distinct wave-front morphologies and enhanced instability tendencies [24]. These results collectively indicate that stratification is not merely an implementation detail of non-premixed fueling, but a first-order factor governing ODW onset and stability.

When the combustor length is constrained, stratification and short residence time compound the initiation difficulty, motivating approaches that actively promote or control onset. Qin et al. proposed exploiting expansion waves downstream of the ramp to facilitate initiation, providing a viable route to reduce the required initiation length under constrained geometries [12]. For more challenging kerosene-class onset, Han et al. demonstrated forced initiation using small surface protuberances on the ramp, suggesting that geometric micro-features can be leveraged to trigger or strengthen ODW formation when mixing and induction are unfavorable [25]. Such efforts underscore that, under non-premixed and length-limited conditions, initiation often requires deliberate flow modulation or localized perturbations to compensate for incomplete mixing and delayed chemistry.

Beyond initiation, non-premixed ODW research has increasingly addressed engineering-scale integration and propulsion-relevant performance. Experimentally, Iwata et al. highlighted the difficulty of stabilizing detonations under non-ideal mixing and off-stoichiometric conditions, underscoring the gap between idealized initiation concepts and practical fueling [26]. Toward integrated ODE configurations, Du et al. indicated that suitable combinations of wall injection and a central strut can meet mixing requirements and enable stabilized ODW formation [27]. Moreover, for ODWs induced by transverse jets, Han et al. decomposed the flow structure and propulsive performance, showing that thrust can arise both from a two-stage compression–reaction pathway (oblique shock followed by detonation) and from trajectories that directly intersect the ODW leading edge [28]. Overall, progress has been made in characterizing mixing non-uniformity, developing initiation control strategies, and extending to practical fuels; however, once the flow is constrained by the channel geometry, a unified and testable quantification is still lacking for how confinement-induced wave reflections, viscous/shear-layer dynamics, and localized chemistry interact under stratified non-premixed inflow to jointly govern the subsequent evolution and stabilized topology.

Despite advances in mixing non-uniformity, initiation control, and practical fuels, the mechanism linking confinement-induced wave reflections, viscous/shear-layer dynamics, and localized chemistry under stratified non-premixed inflow remains insufficiently quantified. Existing studies indicate that, in constrained geometries, ODW interactions with wall boundary layers can induce separation, choking, and wave-system reconfiguration, which may trigger mode transitions and even detonation failure. Sun systematically elucidated

separation-zone evolution driven by ODW/boundary-layer interaction, demonstrated its governing role in wave-system type and stability, and proposed an inviscid Mach–stem-height ratio to characterize wave-system classification and destabilization routes under viscous effects [29–31]. Engineering-oriented ODEs must further account for the coupled impact of injection/mixing, pre-combustion, viscous losses, and nozzle interaction on overall performance 10. For kerosene-fueled ODEs, Suryanarayan et al. discussed how pre-injection and geometric parameters affect initiation and the stability window and provided feasible ranges for ramp angle and ramp height [32]. Tang et al. analyzed the flow field and performance of a Mach 10 kerosene ODE with internal injection under conditions closer to practical operation and examined the coupling among mixing, pre-combustion, and wave-system structure [33]. Recent reviews have noted that experimental research on ODWs for propulsion applications continues to develop, with initiation criteria, structural diagnostics, and control of non-uniform inflows as key directions [34].

Against this backdrop, a key question that remains insufficiently addressed in the ODW/ODE literature is not merely whether an ODW can be initiated under non-premixed fueling in a constrained channel but what physically drives the post-onset pressure evolution once confinement effects become active. In constrained, stratified non-premixed inflow, the secondary pressure rise can plausibly originate from two competing mechanisms—(i) aerodynamically driven recompression associated with confinement-induced reflection/shock-train structures and viscous/shear-layer evolution or (ii) chemically driven pressure gain dominated by localized heat release and wave reorganization—yet these mechanisms may produce similar pressure traces and stabilized morphologies when assessed only in an integral sense. Consequently, prior non-premixed ODW studies, which often emphasize initiation boundaries or qualitative morphology changes, still lack a quantitative, trajectory-resolved attribution of the post-onset pressure rise under strongly stratified inflow [35].

To address this gap, we study a kerosene surrogate fuel, $C_{10}H_{22}$, injected transversely into a Mach-8 constrained supersonic channel representative of engineering ODE combustors, and we quantify (i) how limited mixing and stratification, together with confinement-induced reflections, establish combustor-inlet loss and inhomogeneity and (ii) how the ensuing ODW exhibits a pressure-gain sequence that can be decomposed into primary compression, a pressure plateau, and a secondary pressure-rise stage. We further compare the stabilized ODW morphology and key detonation parameters across three inducer–ramp angles to delineate geometric sensitivity under the same non-premixed, constrained environment. To analyze the static-pressure gain, we introduce a pressure-gradient criterion to identify the recompression segment and employ two trajectory-based, nondimensional metrics: $\Delta x/H$, the normalized misalignment distance between the recompression center and the primary heat-release peak, and $R_{Q,rc}$, the fraction of total heat release contributed within the recompression segment. These metrics enable a quantitative interpretation of whether the secondary pressure rise is primarily associated with recompression or with localized heat release. Finally, direct-connect hot-fire experiments are used to provide a qualitative comparison with the predicted ODW morphology and stabilization trend, thereby offering experimental support for the ramp-angle-dependent wave-topology evolution discussed in this study.

2. Mathematical Model and Experimental System

2.1. Numerical Method

Numerical simulations of the oblique-detonation flow field were performed using the density-based solver rhoReactingCentralFoam in OpenFOAM v7 (The OpenFOAM Foundation Ltd., London, UK) [36,37]. The governing equations are the compressible

multi-species Navier–Stokes equations with finite-rate chemistry, including conservation of mass, momentum, total energy, and species. The continuity equation is written as

$$\frac{\partial \rho}{\partial t} + \nabla \cdot (\rho \mathbf{U}) = 0 \tag{1}$$

where ρ is the density and $\mathbf{U} = (u, v)$ is the velocity vector.

The momentum equation includes the divergence of the effective stress tensor:

$$\frac{\partial (\rho \mathbf{U})}{\partial t} + \nabla \cdot (\rho \mathbf{U} \otimes \mathbf{U}) + \nabla p = \nabla \cdot \boldsymbol{\tau}_{\text{eff}} \tag{2}$$

$$\boldsymbol{\tau}_{\text{eff}} = \mu_{\text{eff}} \left[\nabla \mathbf{U} + (\nabla \mathbf{U})^T - \frac{2}{3} (\nabla \cdot \mathbf{U}) \mathbf{I} \right] \tag{3}$$

$$\mu_{\text{eff}} = \mu + \mu_t \tag{4}$$

where $\boldsymbol{\tau}_{\text{eff}}$ is the effective stress tensor, $\mathbf{I}$ is the identity tensor, μ is the molecular dynamic viscosity, and μ_t is the eddy viscosity provided by the turbulence model

The energy equation is written in terms of the e_s (sensible internal energy), and thermodynamic closure is provided by the selected property model: The energy conservation equation is

$$\frac{\partial (\rho e_s)}{\partial t} + \nabla \cdot (\rho \mathbf{U} e_s) = -p \nabla \cdot \mathbf{U} + \boldsymbol{\tau}_{\text{eff}} : \nabla \mathbf{U} - \nabla \cdot \mathbf{q}_{\text{eff}} + S_e \tag{5}$$

where $-p \nabla \cdot \mathbf{U}$ is the compression work, $\boldsymbol{\tau}_{\text{eff}} : \nabla \mathbf{U}$ is the viscous dissipation, $\mathbf{q}_{\text{eff}}$ is the effective heat flux, and S_e denotes the energy source term associated with chemical heat release/absorption and thermochemical coupling.

Finite-rate chemistry is integrated with a stiff ODE solver and coupled to the flow field via operator splitting; turbulence–chemistry interaction is represented using the PaSR closure. Specifically, the chemistry was solved using the ode chemistry solver with the standard method and the rodas23 stiff ODE solver; the initial chemical time step was set to 1.0×10^{-10}, with absolute and relative tolerances of 1.0×10^{-11} and 1.0×10^{-3}, respectively. In the present PaSR formulation, the finite-rate chemical source term is corrected by the reacting fraction κ, which represents the fraction of each computational cell that is effectively involved in chemical reaction [38,39]. The reacting fraction is evaluated as

$$\kappa = C_\kappa \frac{\tau_c}{\tau_c + \tau_{\text{mix}}} \tag{6}$$

where τ_c is the local chemical time scale obtained from the finite-rate chemistry solver, and τ_{mix} is the turbulent mixing time scale. In the present implementation, the turbulent mixing time scale is calculated as

$$\tau_{\text{mix}} = C_{\text{mix}} \sqrt{\frac{\mu_{\text{eff}}}{\rho \varepsilon}} \tag{7}$$

where μ_{eff} is the effective dynamic viscosity, and ε is the turbulent dissipation rate obtained from the k-ω SST turbulence model. The PaSR constants are set as $C_{\text{mix}} = 0.147$ and $C_\kappa = 1.0$. Therefore, the local reaction source term is controlled by both the finite-rate chemical time scale and the turbulent mixing time scale.

In this study, $C_{\text{mix}} = 0.147$ was adopted as a fixed PaSR mixing-time-scale coefficient commonly used in OpenFOAM-based reacting-flow simulations. This value was kept unchanged for all cases to ensure consistency among different ramp-angle conditions and to avoid case-dependent adjustment of the turbulence–chemistry interaction model.

In addition, no extra empirical correction was applied to the reacting fraction calculated by the standard PaSR formulation, which is equivalent to setting $C_\kappa = 1.0$.

Within each control volume, chemical reactions are represented by a set of ordinary differential equations and integrated in time to obtain the reaction source terms:

$$\boldsymbol{\tau}_{\text{eff}} : \nabla \mathbf{U} = \sum_{i=1}^{2} \sum_{j=1}^{2} \tau_{\text{eff},ij} \frac{\partial U_i}{\partial x_j} \tag{8}$$

$$\mathbf{q}_{\text{eff}} = -\lambda_{\text{eff}} \nabla T \tag{9}$$

Here, $i, j = 1, 2$ corresponds to the x- and y-directions, respectively. The effective thermal conductivity $-\lambda_{\text{eff}}$ accounts for both molecular heat conduction and turbulent thermal diffusion.

This equation represents the transport equation of species mass fraction Y_k. Here, $\mathbf{J}_k$ is the diffusive flux and $\dot{\omega}_k$ is the chemical reaction source term.

$$\frac{\partial(\rho Y_k)}{\partial t} + \nabla \cdot (\rho \mathbf{U} Y_k) = -\nabla \cdot \mathbf{J}_k + \dot{\omega}_k \tag{10}$$

Turbulence is modeled in the Reynolds-averaged Navier–Stokes (RANS) framework using the k-ω SST model [40]. The eddy viscosity μ_t is obtained by solving the transport equations for the turbulent kinetic energy k and the specific dissipation rate ω and is added to the molecular viscosity to form the effective viscosity, $\mu_{\text{eff}} = \mu + \mu_t$, thereby closing the effective stress tensor $\boldsymbol{\tau}_{\text{eff}}$ in the momentum equation. The influence of turbulence on energy transport is incorporated into the heat-flux term $\mathbf{q}_{\text{eff}}$ via $-\lambda_{\text{eff}}$, which is evaluated using parameters such as the turbulent Prandtl number. The molecular viscosity is computed using Sutherland's law, given by

$$\mu = \frac{A_S T^{3/2}}{T + T_S} \tag{11}$$

Here, A_S denotes the reference viscosity constant and T_S is the Sutherland temperature constant. In the present work, A_S = 1.512 × 10^{-6} kg/(m·s) and T_s = 120 K.

For the *k*-*ω* SST model, the fuel-inlet turbulent kinetic energy was specified using the turbulentIntensityKineticEnergyInlet boundary condition with a turbulence intensity of $I_f = 0.10$. The specific dissipation rate was specified using the turbulentMixingLength-FrequencyInlet boundary condition with a turbulent mixing length of $l_f = 1.0 \times 10^{-5}$. Therefore, the fuel-inlet turbulence quantities were specified through turbulence-intensity- and mixing-length-based inlet conditions rather than as fixed uniform k and ω values.

The governing equations are discretized using the finite-volume method. Time integration employs a first-order Euler scheme. Convective fluxes are evaluated using the Kurganov numerical flux. The gradient and diffusion terms are discretized with the Gauss linear scheme, and the diffusion term is treated with the uncorrected option to enhance robustness on complex meshes. Species convection is discretized using Gauss vanLeer01, while the convection of turbulence variables employs bounded Gauss upwind to ensure boundedness and numerical stability.

RP-3 aviation kerosene is represented by a surrogate fuel $C_{10}H_{22}$, and chemical kinetics are described by an 11-species, 10-step elementary mechanism, as shown in Table 1 [27,41,42]. To check the thermodynamic consistency of the adopted mechanism, the CJ detonation parameters of the stoichiometric gaseous $C_{10}H_{22}$–air mixture were calculated under the standard initial condition. The calculated D_{CJ}, p_{CJ}, and T_{CJ} are 1814.75 m/s, 1.959 MPa, and 3118.59 K, respectively, with relative deviations of 5.73%, 6.13%, and 5.40% from the theoretical CJ values. This comparison provides an auxiliary validation for the adopted reduced mechanism.

Table 1. 11-species, 10-step chemical kinetic mechanism.

Reaction	A/(1/s)	B	E/(J/kmol)
$C_{10}H_{22} + O_2 = 10CO + 12H + O_2$	1×10^{12}	0	3.1×10^4
$CH + O_2 = CO + OH$	2×10^{15}	0	3×10^3
$CH + O = CO + H$	3×10^{12}	1	0
$H_2 + O_2 = H_2O + O$	3.98×10^{11}	1	4.8×10^4
$H_2 + O = H + OH$	3×10^{14}	0	6×10^3
$H + O_2 = O + OH$	4×10^{14}	0	1.8×10^4
$H_2O + O_2 = 2O + H_2O$	3.17×10^{12}	2	1.12×10^5
$CO + OH = CO_2 + H$	5.51×10^7	1.27	-7.58×10^2
$CO + H_2O = CO + H_2$	5.5×10^4	1.27	-1×10^3
$CO + H_2 + O_2 = CO_2 + H_2O$	1.6×10^{14}	1.6	1.8×10^4

To further assess the induction-time prediction capability of the adopted $C_{10}H_{22}$/air reduced mechanism, a 0-D ignition-delay-time validation was performed using the Closed Homogeneous Reactor module in ANSYS Chemkin-Pro 2019 (ANSYS, Inc., Canonsburg, PA, USA). Since RP-3 aviation kerosene is represented by a gaseous $C_{10}H_{22}$ surrogate in the present simulations, the ignition-delay calculation was conducted for the gas-phase surrogate-fuel/air mixture rather than for liquid RP-3 spray ignition. Therefore, physical processes such as atomization, evaporation, droplet transport, and two-phase heat and mass transfer were not included in this validation.

Two representative constant-pressure conditions were selected for the calculation, namely T = 1800 K, p = 140 kPa, ER = 1.0, and T = 2200 K, p = 100 kPa, ER = 1.0. The ignition delay time was defined as the time corresponding to the maximum temperature-rise rate, i.e., peak dT/dt, in the homogeneous reactor. The temperature–time histories are shown in Figure 1, and the extracted ignition delay times are summarized in Table 2. To provide a quantitative reference, the ignition delay times predicted by the present reduced mechanism were compared with the reference values obtained from the empirical correlation fitted from the RP-3 experimental ignition-delay data reported by Chen et al. [43]. As shown in Table 2, the calculated ignition delay times are 0.0295 ms and 0.0210 ms for the two conditions, respectively, while the corresponding reference values are 0.0308 ms and 0.0202 ms. The relative errors are 4.22% and 3.66%, respectively. These deviations are within 5%, indicating that the present reduced mechanism can reasonably reproduce the gas-phase chemical induction time scale of the surrogate fuel under the high-temperature and low-pressure conditions relevant to this study. Together with the CJ detonation-parameter comparison, the added 0-D ignition-delay assessment further supports the applicability of the reduced mechanism for the trend-level analysis of gas-phase surrogate-fuel ODW initiation and stabilization.

In the present simulation, RP-3 aviation kerosene is represented by a gaseous $C_{10}H_{22}$ surrogate. The fuel is directly introduced as a gas-phase species at the inlet, and liquid-fuel atomization, droplet breakup, evaporation, and two-phase spray dynamics are not considered. This simplification allows the present study to focus on gas-phase fuel–air mixing, shock compression, finite-rate chemistry, and ODW initiation/stabilization in the constrained combustor. Therefore, the results should be interpreted as gas-phase surrogate-fuel predictions. When applying the conclusions to practical liquid RP-3 injection, additional effects associated with atomization quality, droplet evaporation, spray penetration, droplet inertia, and two-phase momentum/heat transfer should be further considered.

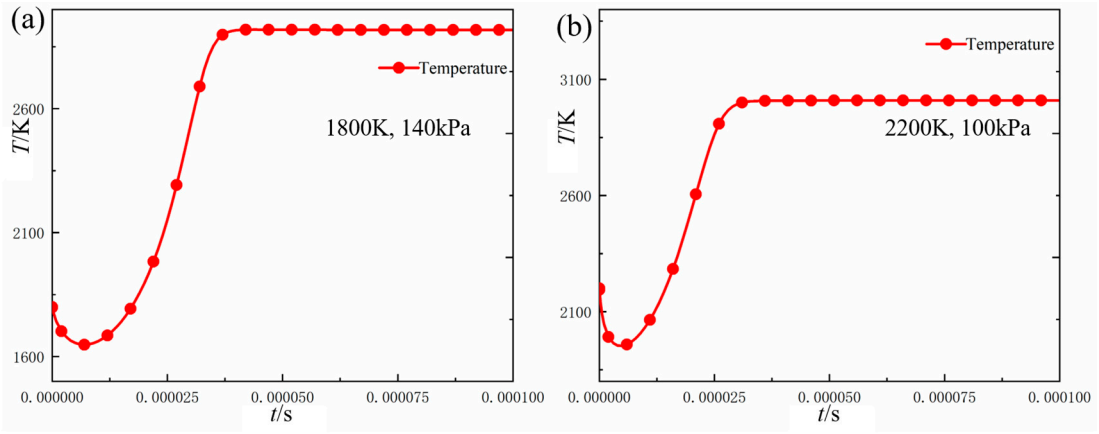

Figure 1. Ignition-delay-time validation of the reduced $C_{10}H_{22}$/air mechanism based on temperature–time histories in a 0-D constant-pressure homogeneous reactor: (**a**) T = 1800 K, p = 140 kPa, ER = 1.0; (**b**) T = 2200 K, p = 100 kPa, ER = 1.0.

Table 2. Comparison of ignition delay times between the present reduced mechanism and literature reference data.

Case	Calculated Ignition Delay Time/ms	Reference Value/ms	Relative Error
1800 K, 140 kPa	0.0295	0.0308	4.22%
2200 K, 100 kPa	0.0210	0.0202	3.66%

2.2. Physical Model and Simulation Conditions

To investigate fuel injection/mixing and detonation initiation in a constrained hypersonic configuration, the computational model shown in Figure 2a is employed. The configuration consists of an injection section, a mixing section, and a combustor, with a channel height of $H = 150$ mm. Figure 2b shows the computational mesh. To satisfy the low-y^+ near-wall treatment required by the k–ω SST model, the first-layer mesh height was specified to keep $y^+ \approx 1$ on all solid walls.

In the numerical simulations, a Mach 8 inflow representative of a 30 km altitude flight condition is considered. Temperature-dependent thermodynamic properties are evaluated using NASA seven-coefficient polynomials, and the mixture is treated as a thermally perfect gas. After inlet compression, the air inflow conditions at the injection-section inlet are summarized in Table 3.

Table 3. Air inflow conditions at the injection-section inlet.

Parameter	Value
Flight Mach number/Ma	8
Flight altitude/km	30
Inlet Flight Mach number at the mixing section/Ma	4
Inlet pressure at the mixing section/kPa	26.266
Inlet temperature at the mixing section/K	755
Inlet velocity at the mixing section/(m/s)	2285

Under the above air-inflow condition, RP-3 aviation kerosene was introduced through transverse fuel injection to form a non-premixed fuel–air mixture before entering the combustor. In the numerical model, RP-3 was represented by a gaseous $C_{10}H_{22}$ surrogate, and the global equivalence ratio was set to $\phi_g = 1.0$. The fuel-inlet boundary was implemented as a pressure-dependent compressible inflow condition using the groovyBC function in

swak4Foam, rather than as a fixed-velocity or fixed-mass-flow inlet. The nominal fuel stagnation pressure and stagnation temperature were $p_{0,f} = 2.0$ MPa and $T_{0,f} = 300$ K, respectively. During the calculation, the local injection velocity and thermodynamic state at the fuel inlet were automatically adjusted according to the local back pressure adjacent to the injection boundary. Therefore, the fuel mass-flow rate was not independently imposed as a constant value but was determined by the pressure-dependent inlet condition and evaluated from the surface-integrated normal mass flux at the fuel inlet.

The time step is adaptively adjusted to satisfy a CFL constraint, with a maximum CFL number of 0.5 enforced in the core flow region. Chemical source terms are integrated with a stiff ODE solver and coupled to the flow equations via operator splitting to control reaction-integration errors at each time step. All walls are modeled as no-slip and adiabatic.

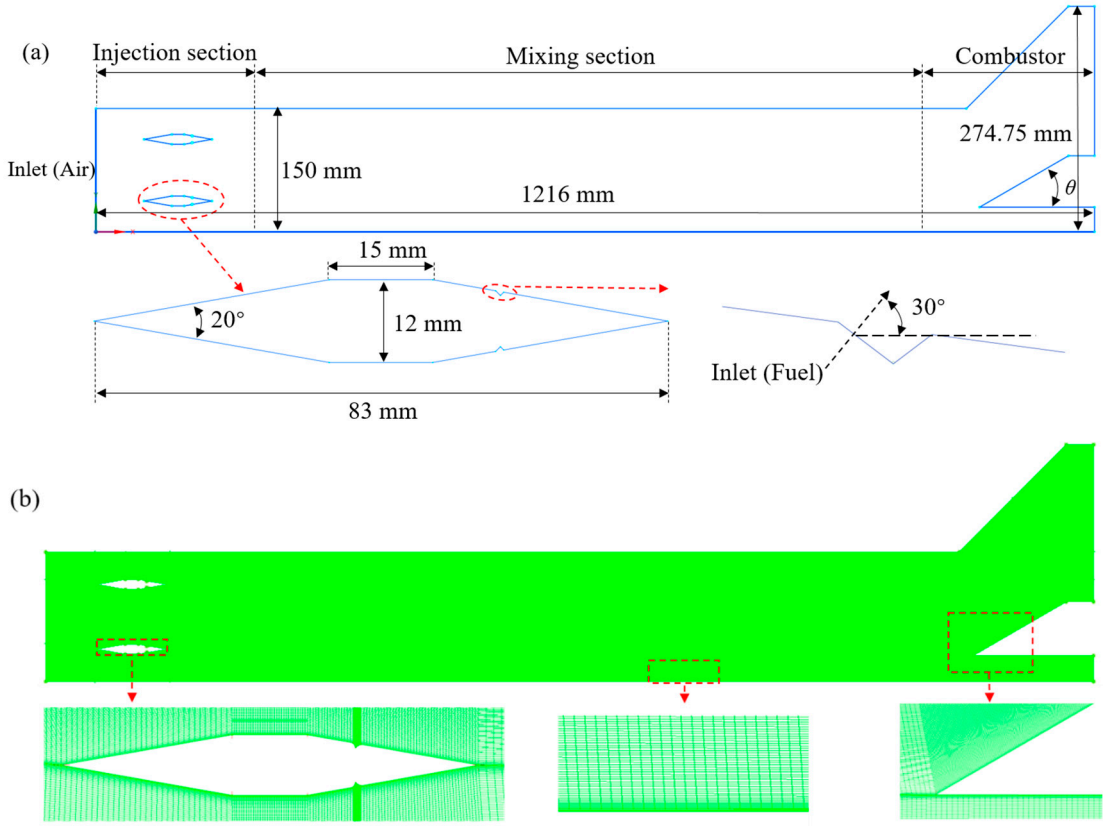

Figure 2. Computational configuration and mesh generation: (**a**) computational model for oblique-detonation combustion organization in a constrained domain; (**b**) computational-domain mesh and near-wall refinement.

2.3. Validation of the Numerical Model and Grid Independence

To assess the baseline capability of the present methodology for hypersonic reacting flows involving strong shock compression and rapid heat release, we considered the canonical hypervelocity-projectile-induced-shock-induced-combustion experiment reported by Lehr [44,45]. In the Lehr configuration, a projectile with a blunt nose diameter of 15 mm is considered. The incoming flow is a premixed combustible mixture with an initial temperature of 293 K, an inflow Mach number of 3.55, and an initial static pressure of 42.665 kPa. To focus on the coupled shock-layer/reaction-zone features while maintaining computational efficiency, the computational domain is restricted to a local region covering 2.5 mm upstream of the nose and 10 mm in the transverse (upper) direction.

Figure 3a shows the computed temperature field, and Figure 3b compares the centerline ($y = 0$) pressure and temperature gains between the simulations and Lehr's measure-

ments. The simulations reproduce the characteristic wave structure ahead of the projectile and yield centerline pressure/temperature gains in good agreement with the measurements. These comparisons support the suitability of the present solver for shock-induced combustion under supersonic inflow conditions.

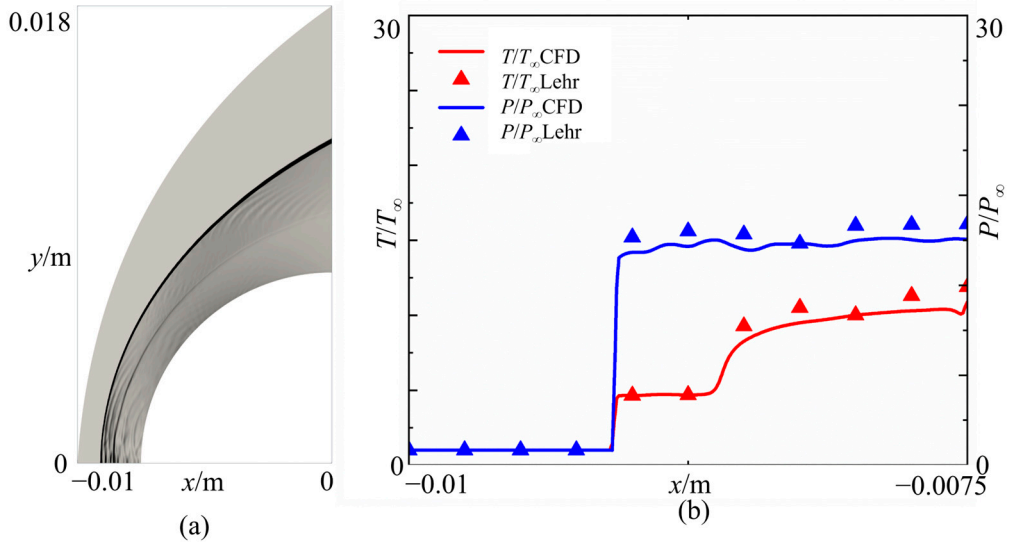

Figure 3. Comparison between the numerical simulation and experimental results for Lehr's high-speed-projectile-induced detonation initiation: (**a**) numerical schlieren image; (**b**) comparison of pressure and temperature gains obtained from the experiment and simulation.

The Lehr blunt-body case has been widely adopted as a standard validation benchmark in numerical studies of ODW initiation and stabilization, including recent studies on hydrogen-fueled pre-injection combustors and jet–wedge combinatorial ODW initiation [46]. Therefore, it is used here as a canonical validation of the basic shock-induced reacting-flow capability of the numerical method, rather than as a complete validation of the present Ma8, non-premixed, RP-3-fueled constrained-channel combustor.

Considering the remaining differences in fuel type, inflow stratification, and confinement-induced wave interactions, the present validation is used to support the qualitative reliability of the predicted ODW morphology and stabilization trend, rather than to claim a fully quantitative validation of all local reacting-flow details.

To further assess the applicability of the present numerical method to a flow regime closer to the constrained-channel ODE configuration considered in this study, an additional validation case was supplemented based on our previous work [47]. This validation case involves transverse fuel injection, supersonic fuel–air mixing, and ramp-induced oblique-detonation initiation in a confined combustor. Compared with the Lehr blunt-body benchmark, this configuration contains physical processes more directly related to the present study, including jet–crossflow interaction, confined-channel wave reflection, ramp-induced compression, and oblique-detonation initiation.

The present numerical method was applied to this confined-space ODE validation case, and the computed pressure and temperature distributions along a representative combustor streamline passing through $x = 1.0$ mm and $y = 0.055$ mm were compared with the corresponding reference results. As shown in Figure 4, the present results agree well with the reference data in terms of the main pressure-rise trend and temperature-response behavior. The maximum relative error of pressure is 2.481%, and the average relative error of temperature is 3.351%. These results indicate that the numerical model established in this study can reasonably reproduce the main pressure-rise and temperature-variation

characteristics associated with fuel-injection mixing and ramp-induced oblique-detonation initiation in a confined combustor.

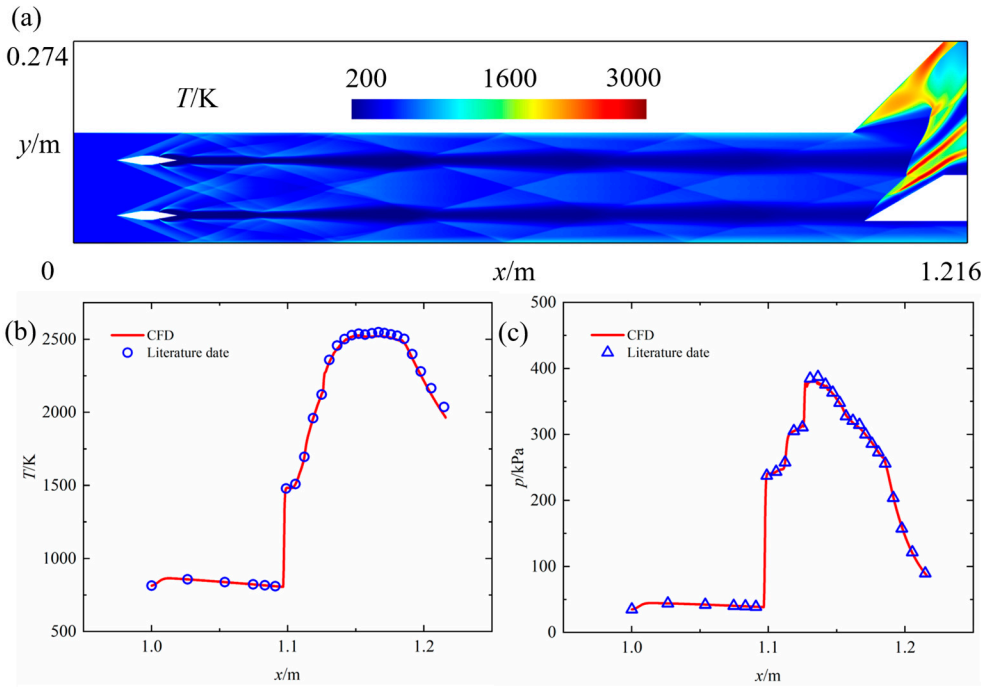

Figure 4. Validation of the numerical model for fuel-injection mixing and ramp-induced oblique-detonation initiation in a confined combustor: (**a**) temperature contour of the hydrogen validation case; (**b**) comparison of temperature distributions along the representative combustor streamline; (**c**) comparison of pressure distributions along the representative combustor streamline.

Therefore, the validation strategy in the present work contains two complementary levels. The Lehr blunt-body case is used to verify the baseline capability of the solver for shock-induced reacting flows, while the confined-space ODE validation case provides additional support for the applicability of the present numerical method to fuel-injection mixing and ramp-induced oblique-detonation initiation. Nevertheless, because the additional validation case is based on a hydrogen-fueled configuration, whereas RP-3 aviation kerosene is represented by a gaseous $C_{10}H_{22}$ surrogate in the present simulations, the validation is used to support the qualitative and trend-level reliability of the predicted initiation and stabilization behavior rather than to claim complete quantitative validation of all local reacting-flow details.

For the present computational model, simulations were performed using three nominal grid sizes of 0.25 mm, 0.375 mm, and 0.5 mm. The influence of grid resolution was first evaluated by comparing the pressure and temperature distributions along the ramp surface in the combustor, as shown in Figure 5. The results indicate that the grid size has a certain influence on the ramp-surface temperature and pressure distributions. However, when the grid size is 0.375 mm, further refinement to 0.25 mm produces only minor changes in the ramp-surface pressure and temperature profiles, indicating that the 0.375 mm grid can reasonably capture the main flow-field characteristics in the combustor.

To further evaluate the grid sensitivity of the detonation-region characteristics, two additional ODW-related indicators were extracted from the stabilized 30° ramp case: the ODW anchoring position and the ODW wave angle. The ODW anchoring position was determined from the first major simultaneous rise in wall pressure and wall temperature along the ramp surface. The ODW wave angle was defined as the angle between the foremost leading oblique shock/ODW-coupled front and the incoming main-flow direction

in the stabilized flow field. The wave-front was identified from the pressure-gradient field as the continuous high-gradient ridge corresponding to the leading coupled compression/reaction front. The fitting interval was selected from the quasi-linear portion of this ridge downstream of the anchoring point, while excluding the influence of local high-gradient structures associated with the near-wall anchoring region, reflected shocks, transverse waves, and triple-point disturbances. The ODW wave angle was then obtained by linearly fitting the extracted wave-front points within this interval. As summarized in Table 4, the ODW anchoring positions obtained with grid sizes of 0.25 mm, 0.375 mm, and 0.5 mm are 1.10198 m, 1.10220 m, and 1.10642 m, respectively. The corresponding ODW wave angles are 46.1°, 46.3°, and 44.2°, respectively. Compared with the 0.25 mm grid, the 0.375 mm grid gives close predictions of both the anchoring position and the wave angle, whereas the 0.5 mm grid shows a more noticeable deviation. Therefore, considering both computational accuracy and computational cost, the 0.375 mm grid is adopted for all subsequent simulations in this study.

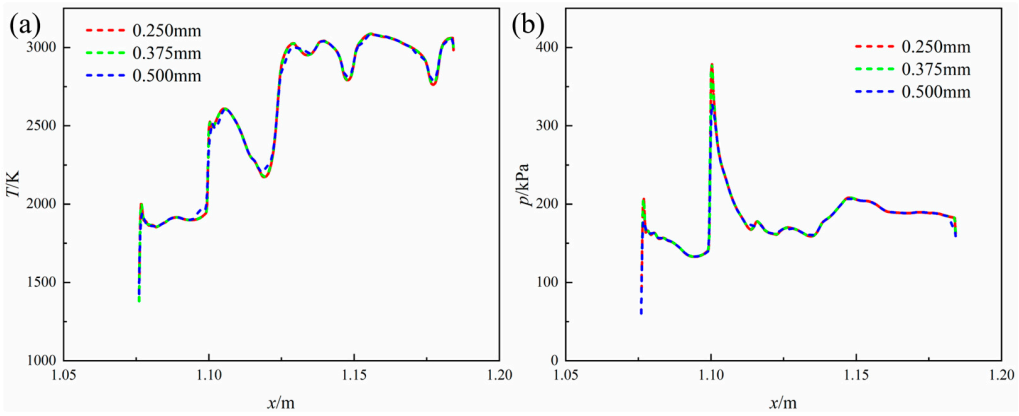

Figure 5. Pressure and temperature distributions along the combustor ramp surface under different grid sizes. (**a**) Temperature distribution curve; (**b**) pressure distribution curve.

Table 4. Comparison of ODW anchoring position and shock angle under different grid resolutions and CFL numbers.

Case	Value	ODW Anchoring Position/m	ODW Angle/°
Grid size1/mm	0.25	1.10198	46.1
Grid size2/mm	0.375	1.10220	46.3
Grid size3/mm	0.5	1.10642	44.2
$CFL_{max}1$	0.5	1.10220	46.3
$CFL_{max}2$	0.1	1.10241	46.2

In addition, a CFL-number sensitivity check was performed by comparing the results obtained with maximum CFL numbers of 0.5 and 0.1 using the 0.375 mm grid. As shown in Figure 6, the pressure and temperature distributions along the ramp surface show no noticeable difference under the two CFL limits. The ODW-related indicators in Table 4 further confirm this conclusion. The ODW anchoring positions obtained with $CFL_{\max} = 0.5$ and $CFL_{\max} = 0.1$ are 1.10220 m and 1.10241 m, respectively, and the corresponding ODW wave angles are 46.3° and 46.2°. These differences are very small, indicating that the predicted ODW anchoring behavior and wave angle are not sensitive to the time-step restriction within the tested range. Therefore, the maximum CFL number is kept below 0.5 in the present simulations.

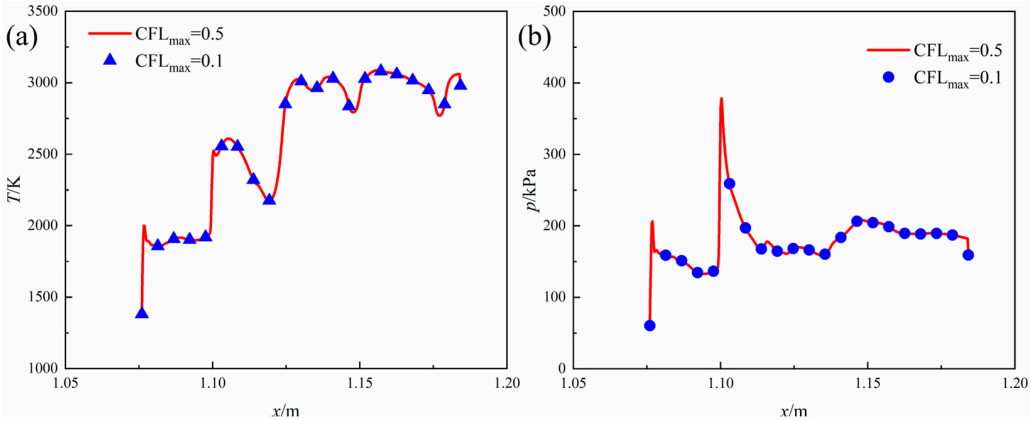

Figure 6. Pressure and temperature distributions along the combustor ramp surface under different $CFL_{\max}$ values. (**a**) Temperature distribution curve; (**b**) pressure distribution curve.

2.4. Experimental System and Diagnostic Method

To assess the applicability of the present methodology to hypersonic reacting flows with strong shock compression and rapid heat release, we consider the canonical blunt-body-induced oblique-detonation case.

To provide an experimental assessment of the ramp-angle-dependent initiation threshold, global wave topology, and stabilized-front behavior predicted by the simulations, direct-connect hot-fire tests were conducted using an oblique-detonation-engine combustor model. It should be noted that the experiments were not intended to provide pointwise validation of the computed pressure, temperature, or heat-release fields. Instead, they were used as an independent qualitative check of the initiation mode, global wave morphology, and stabilized-front behavior for the three ramp angles considered in the numerical study.

A schematic of the experimental system is shown in Figure 7. The test was performed in a ground-based direct-connect facility that supplied a high-enthalpy airflow corresponding to the nominal Mach-8/30 km altitude condition used in the simulations. The total temperature and total pressure of the airstream were $T_{0,air}$ = 2696.8 K and $p_{0,air}$ = 17.3 MPa, respectively. The combustor model consisted of a constrained supersonic channel, a transverse fuel-injection section, and an interchangeable inducer ramp. The main geometric dimensions of the experimental model, including the channel height, channel width, mixing-section length, combustor length, injector location, and ramp installation position, were strictly consistent with those used in the numerical model. To examine the effect of geometric compression strength on ODW initiation and stabilization, three ramp angles, 25°, 30°, and 35°, were tested under otherwise identical operating conditions.

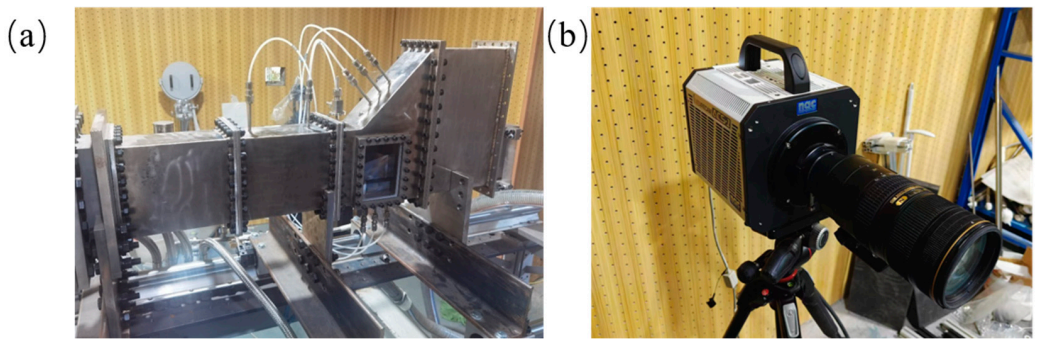

Figure 7. Ground direct-connect test and observation setup for the oblique detonation engine. (**a**) Ground direct-connect test rig for the oblique-detonation engine; (**b**) high-speed imaging system.

In the experiments, RP-3 aviation kerosene was supplied through the transverse injector, whereas in the numerical simulations it was represented by a gaseous $C_{10}H_{22}$ surrogate. The global equivalence ratio of the experimental condition was $\phi_g = 1.0$. Because atomization, vaporization, wall wetting, and multi-component real-fuel effects are not resolved in the present numerical model, the experimental comparison is used primarily to evaluate the global initiation trend and wave morphology rather than detailed local ignition-delay, mixing, or intermediate-species characteristics.

The wave structure and temporal evolution in the combustor were recorded through an optical window using a high-speed imaging system at an acquisition frequency of 20 kHz. The image sequence was used to identify the global wave-front location, the presence or absence of a stabilized oblique front, and the temporal steadiness of the wave morphology. Since no calibrated temperature, species, or pressure field was extracted from the optical images, the experimental results should be interpreted as qualitative morphology validation rather than complete quantitative validation of all computed flow variables.

3. Results and Discussion

3.1. Characteristics of the Injection and Mixing Process of $C_{10}H_{22}$

Taking the case with a 30° injection angle as an example, we analyze the injection and mixing process of the fuel $C_{10}H_{22}$ in the mixing section. After exiting the injector, the jet is convected downstream by the supersonic main flow and becomes elongated in the streamwise direction. Pronounced velocity and density gradients at the jet–crossflow interface promote shear-layer instability and entrainment. Under supersonic conditions, a bow shock forms upstream of the jet, together with internal jet shocks (barrel shock and Mach disk) and a downstream shock-cell pattern. The interaction between the shock system and the shear layer generates vorticity and enhances entrainment, such that mixing is jointly governed by wave-system modulation and vortical transport. Figure 8 presents instantaneous contours illustrating the temporal evolution of the injection and mixing process of the $C_{10}H_{22}$.

At t = 0.1 ms, the fuel is injected into the mixing section through the two injectors located on the upper and lower sides of the strut. A high-concentration region forms in the near field, accompanied by short-range recirculation and entrainment. At this stage, the jet cores remain constrained near the injection plane, producing a thin mixing layer with limited transverse penetration.

At t = 0.3 ms, the high-speed crossflow elongates both jets into slender streamwise fuel streaks. While a high-concentration core persists near the injectors, a thin concentration-transition layer develops along the jet boundary. Small-amplitude interfacial undulations appear, indicating the onset of Kelvin–Helmholtz-type shear-layer instability. Ambient air is continuously entrained into the shear layer, and the mixing layer thickens downstream.

By t = 0.4 ms, the jet-core length increases further. The oscillation amplitude along the streak edges increases and extends downstream, reflecting intensified shear-layer entrainment and stretching. Meanwhile, the mixing layers of both jets thicken relative to the previous instant, and local crest-like structures emerge, suggesting periodic stripping and downstream transport of fuel-rich packets by coherent vortices.

At t = 0.52 ms, the jets evolve into a more fully developed unsteady mixing stage. In the downstream region, larger-scale and more regular wave-train-like fluctuations are observed. The fuel streaks exhibit pronounced lateral meandering and entrainment-driven spreading. Locally, larger vortical agglomerates undergo a "roll-up–stretching–breakdown" process, promoting stronger diffusion and dilution of the fuel both transversely and streamwise, particularly toward the core-flow passage. Overall, the mixing process evolves from

near-field jet accumulation to streamwise stretching into streaks and finally to enhanced shear-layer undulations with large-scale entrainment.

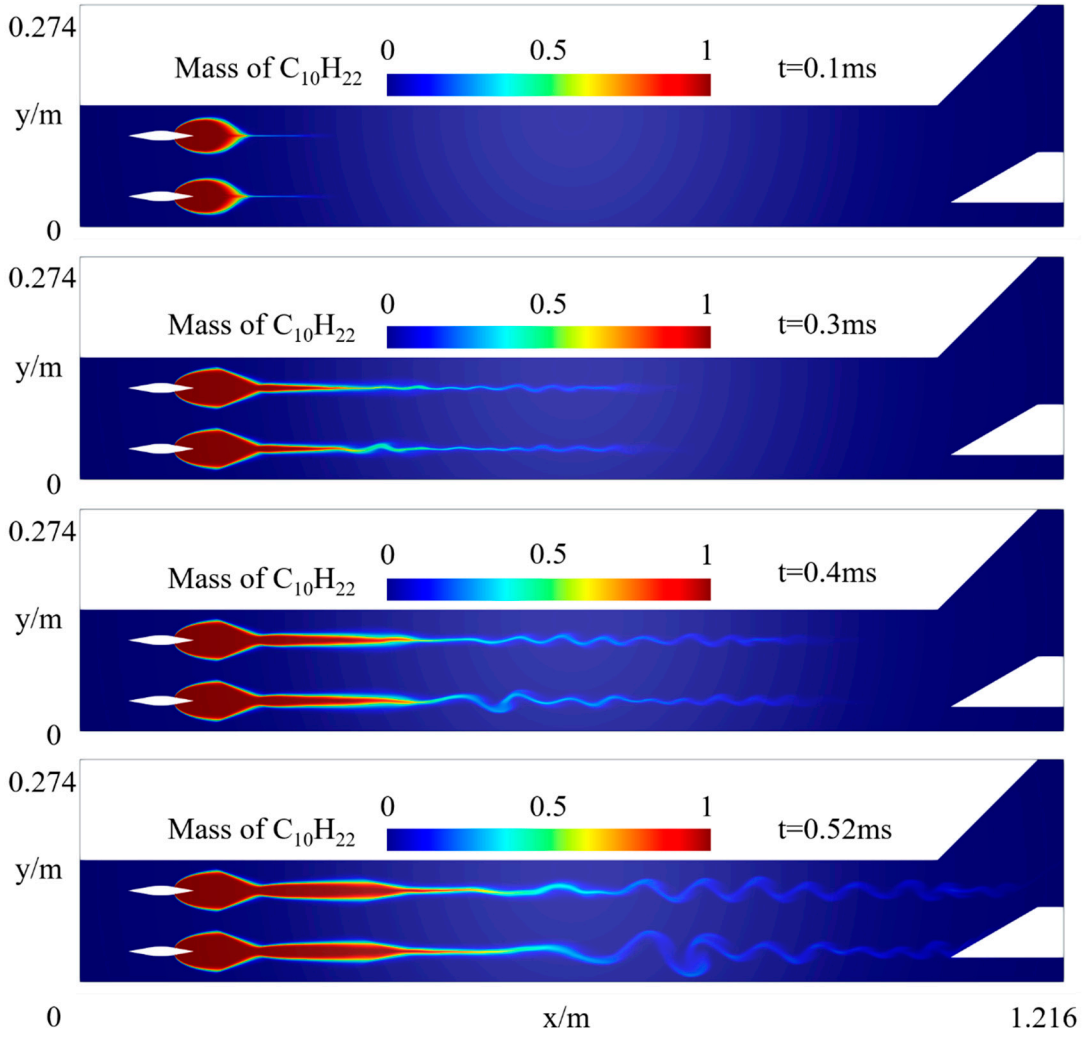

Figure 8. Instantaneous contours of the $C_{10}H_{22}$ field illustrating the temporal evolution during the injection and mixing process.

Figure 9 presents instantaneous temperature and pressure contours at t = 0.52 ms, indicating that the mixing-section flow has evolved into a regime dominated by jet–shock interactions with increasingly pronounced unsteady shear-layer undulations. Near the injectors, the upper and lower jets interact with the crossflow and form a distinct compression region immediately downstream of the injection exits. Farther downstream, a periodic diamond-shaped shock-cell pattern develops: alternating compression and expansion waves form a regular diamond-cell pressure field, which corresponds to alternating high-temperature streaks along the jet axis. This pattern reflects successive over- and under-expanded adjustments of the jets in a supersonic crossflow.

Clear shear interfaces form both between the two jets and between each jet and the outer crossflow. In the near field, oblique compression waves overlap and interact between the upper and lower jets, inducing flow turning; under the constraint of the shock system, the jet cores are continuously stretched in the streamwise direction. In the mid-to-downstream part of the mixing section, the jet boundary in the temperature field transitions from a smooth interface to a wave-train-like pattern, demonstrating the growth of shear-layer instabilities and the associated enhancement of entrainment. Consistently, the regular diamond shock-cell pattern gradually weakens, suggesting progressive dissipation

by turbulent mixing and viscous effects and a transition from a shock-dominated regime toward mixing-dominated transport.

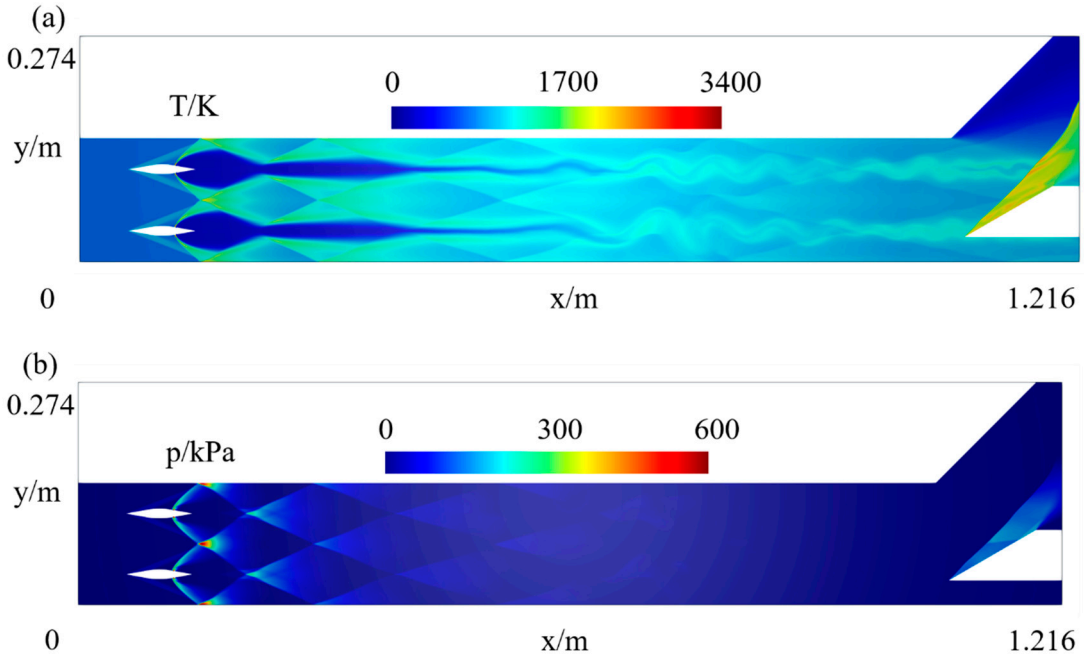

Figure 9. Instantaneous temperature and pressure contours of the flow field: (**a**) Instantaneous temperature contours of the flow field; (**b**) Instantaneous pressure contours of the flow field.

Near the combustor entrance, geometric contraction and flow turning generate a strong oblique-shock compression region. The pressure rises markedly near the leading edge of the ramp, accompanied by a concurrent temperature increase and the formation of a high-temperature band produced by flow compression. The compression waves propagate into the channel and undergo reflection and refraction at the upper and lower walls, resulting in a complex inlet structure involving an oblique shock, reflected waves, and shear layers. This high-pressure/high-temperature precompression environment further modifies the local Mach number and density distributions of the mixture. Owing to these combined effects, the non-premixed mixture exhibits a distribution at the combustor inlet that is fundamentally different from that under premixed inflow conditions.

Figure 10 compares combustor-inlet flow parameters between the non-premixed and premixed cases. The results indicate that the two fueling strategies lead to markedly different inlet boundary conditions at the combustor entrance. Importantly, the difference is not constrained to a single variable; rather, it appears as coupled non-uniformities in composition, thermodynamics, and velocity.

In terms of composition, the non-premixed case features pronounced stratification of fuel mass fraction across the channel height because the fuel is introduced as transverse jets and undergoes convection-driven mixing over a limited length. A relatively high fuel concentration remains within the jet-core region, whereas the mixed layer formed by shear-layer entrainment exhibits a rapid decay in fuel concentration toward the outer edges. Consequently, the inlet plane is characterized by strong gradients and a highly non-uniform coexistence of fuel-rich and fuel-lean regions. By contrast, the premixed case yields an almost constant fuel mass-fraction profile at the inlet, indicating a higher degree of mixing and a more uniform effective equivalence-ratio field. This compositional non-uniformity directly induces spatial variations in chemical reactivity, leading to substantial lateral scatter in local induction time, heat-release intensity, and flammability margin, which in turn exerts

a strong influence on the subsequent stationing location and wave-system structure of the oblique detonation.

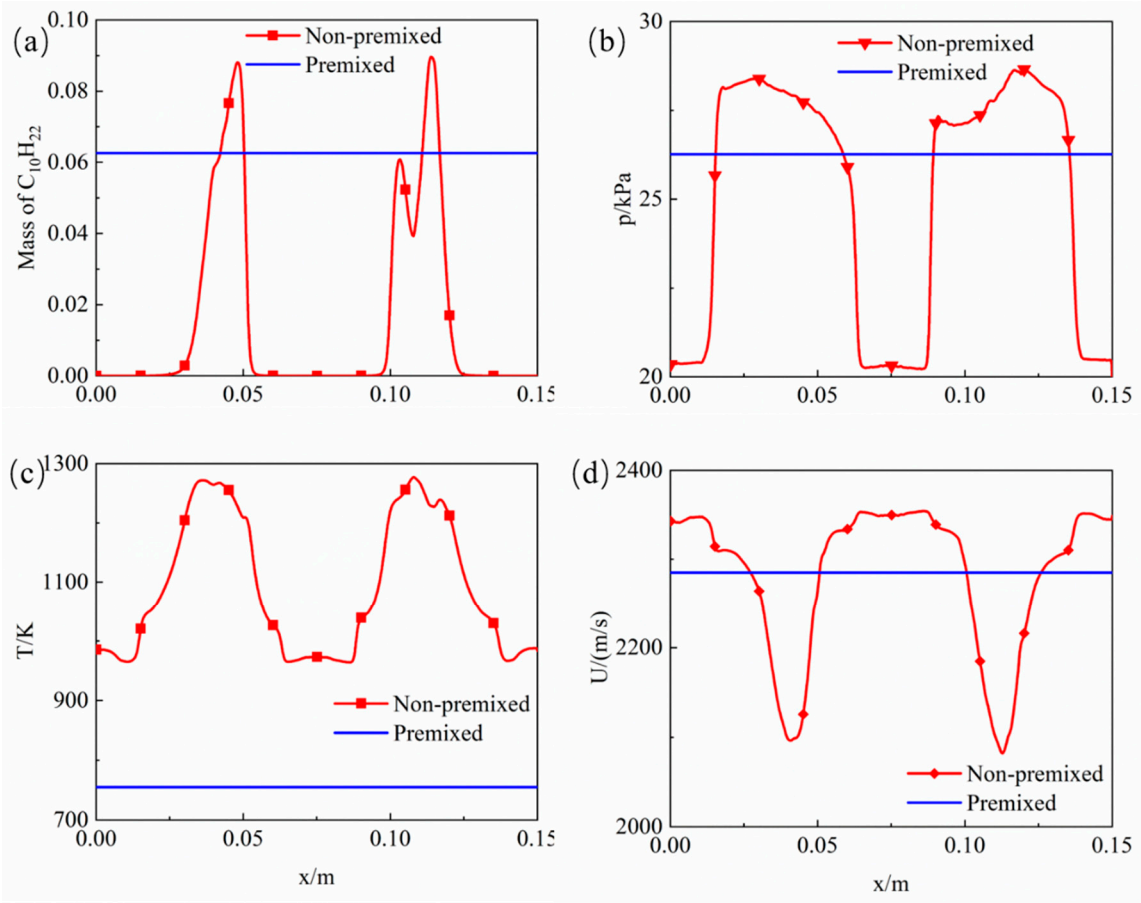

Figure 10. Distributions of flow parameters at the combustor inlet under non-premixed and premixed conditions: (**a**) mass fraction of $C_{10}H_{22}$; (**b**) pressure distribution; (**c**) temperature distribution; (**d**) velocity distribution.

For thermodynamic variables, the non-premixed inlet pressure and temperature profiles exhibit distinct oscillations and plateau-like segments, implying that the compression/expansion wave system generated by jet–crossflow interaction in the mixing section continues to modulate the inlet plane. Local compression elevates pressure and induces compressive heating, producing corresponding high-temperature streaks, whereas expansion leads to a recovery of these quantities. As a result, alternating "high-pressure/high-temperature" and "low-pressure/low-temperature" zones emerge within the same inlet cross-section. In the premixed case, the absence of jet-induced wave structures and strong shear layers yields much smoother pressure and temperature distributions, approaching quasi-one-dimensional inflow characteristics. The velocity field shows a consistent coupled response: in the non-premixed case, pronounced deceleration appears in compression-dominated regions, indicating conversion of kinetic energy into internal energy through irreversible shock losses and turbulent-mixing dissipation; in contrast, the premixed velocity profile varies only mildly, reflecting a more uniform dynamical state.

Overall, the non-premixed inlet boundary condition exhibits multi-scale non-uniformity and strong-gradient features. This enhances the non-uniform and unsteady nature of the inflow encountered by the oblique detonation, making the detonation front more prone to undulations and asymmetric evolution.

To further evaluate the fuel mixing performance downstream of the mixing section, the combustor-inlet location is selected as the assessment position. Since the present simulation is two-dimensional, the combustor-inlet cross-section is represented by an inlet sampling line in the computational plane. Therefore, 1001 uniformly distributed discrete sampling points are arranged along this inlet line to quantitatively analyze the uniformity of the fuel mass-fraction distribution. The intensity of segregation proposed by Danckwerts is adopted as the mixing non-uniformity index [48]. For the fuel mass fraction Y_f at the discrete sampling points along the inlet sampling line, the line-averaged mean value and variance are defined as

$$\overline{Y} = \frac{1}{N}\sum_{i=1}^{N} Y_i \tag{12}$$

$$\sigma_Y^2 = \frac{1}{N}\sum_{i=1}^{N} (Y_i - \overline{Y})^2 \tag{13}$$

where $N = 1001$ is the number of uniformly distributed sampling points along the combustor-inlet line and Y_i is the fuel mass fraction at the i-th sampling point.

In this case, the fuel mass fraction at the combustor inlet is not bounded by ideal pure-stream values of 0 and 1 because the fuel jet has already undergone shear-layer mixing, diffusion, and compression before entering the combustor. Therefore, using ideal end-member values of 0 and 1 to construct the fully segregated variance would introduce an artificial reference state that is not directly attainable on the sampled inlet line. To avoid this bias, the actual end-member values $Y_{\min}$ and $Y_{\max}$ obtained from the 1000 uniformly distributed sampling points are used to define the maximum variance corresponding to a fully segregated distribution within the observed range.

$$\sigma_{Y,0}^{*2} = (\overline{Y} - Y_{\min})(Y_{\max} - \overline{Y}) \tag{14}$$

Accordingly, the intensity of segregation based on the actual end-member values, together with the corresponding mixing uniformity, are defined as follows:

$$I^* = \frac{\sigma_Y^2}{(\overline{Y} - Y_{\min})(Y_{\max} - \overline{Y})} \tag{15}$$

$$\eta^* = 1 - I^* \tag{16}$$

Here, a larger I^* indicates stronger segregation and poorer mixing, whereas η^* approaching unity implies a more uniform fuel distribution. Based on the cross-sectional data at the combustor inlet, $I^* = 0.63171$ and the corresponding mixing uniformity is $\eta^* = 0.36829$, indicating a markedly non-uniform fuel distribution at the combustor entrance.

As an auxiliary indicator, the coefficient of variation in the local equivalence ratio is also calculated along the combustor-inlet sampling line, since equivalence-ratio-based distributions have been used to evaluate fuel–air mixing quality [49]. For the i-th sampling point, the local equivalence ratio is defined as

$$\phi_i = \frac{\left(Y_f / Y_{O_2}\right)_i}{\left(Y_f / Y_{O_2}\right)_{st}} \tag{17}$$

For $C_{10}H_{22}$, this gives $\phi_i \approx 3.486 Y_{f,i}/Y_{O_2,i}$. The coefficient of variation is then defined as

$$CV_\phi = \frac{\sigma_\phi}{\overline{\phi}} \tag{18}$$

where $\bar{\phi}$ and σ_ϕ are the mean value and standard deviation of the local equivalence ratio along the inlet sampling line. The calculated values are $\bar{\phi} = 0.2434$, $\sigma_\phi = 0.4328$, and $CV_\phi = 1.778$. Since $CV_\phi > 1$, the local equivalence-ratio fluctuation exceeds its mean value, confirming a highly non-uniform and strongly stratified fuel–air distribution at the combustor inlet. This result is consistent with the Danckwerts segregation-intensity analysis.

Figure 11 shows the distribution of the total-pressure recovery coefficient in the mixing section. The recovery coefficient decreases monotonically downstream, with an initially mild decline followed by a steeper drop and a gradual approach to a quasi-steady value. Due to shock reflections in the mixing section, the core flow experiences repeated cycles of shock compression and reflection within the channel. Consequently, the total-pressure recovery coefficient continues to decrease and asymptotically approaches 0.49.

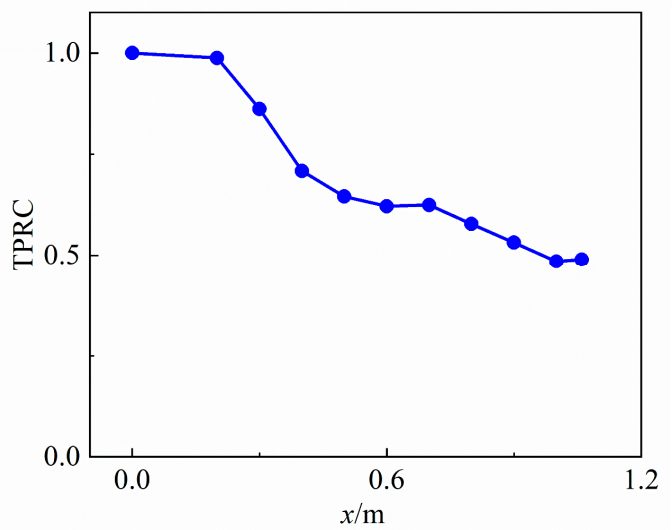

Figure 11. Streamwise distribution of the total-pressure recovery coefficient.

3.2. Initiation and Stabilized Wave-System Structure of an Oblique Detonation in a Constrained Supersonic Channel

Numerical simulations are conducted to investigate oblique-detonation initiation and stabilization in a constrained supersonic channel under a Mach 8 inflow representative of a 30 km altitude condition. The injection angle is 30° (non-premixed, partially mixed inflow), and a 30° ramp is used to provide flow compression. The stabilized state after successful initiation is shown in Figure 12. The numerical schlieren image in Figure 12a depicts the overall topology of the coupled shock/oblique-detonation system in the stabilized state. Figure 12b presents schematic streamlines used to characterize the differences in wave interaction and reaction response along different stratified inflow paths, denoted as line 1, line 2, and line 3. The OH mass-fraction distribution in Figure 12c is used to identify the rapid reaction zone and its spatial coupling with the leading wave system.

To provide auxiliary thermodynamic and dynamic references for identifying the reacting wave structure, the local mixture parameters in the fuel-containing region at the combustor inlet were extracted, and the corresponding theoretical CJ detonation parameters were calculated. In the present analysis, the fuel-containing region was defined as the region with $Y_{C_{10}H_{22}} > 10^{-3}$. The averaged initial state of this region is $Y_{C_{10}H_{22}} = 0.03875$, $Y_{O_2} = 0.21741$, $T_0 = 1101.76$ K, and $p_0 = 26.04$ kPa. Based on this averaged inlet state, the calculated theoretical CJ parameters are $D_{CJ} = 1499.7$ m/s, $p_{CJ} = 100.3$ kPa, and $T_{CJ} = 2472.6$ K, corresponding to a pressure ratio of $p_{CJ}/p_0 = 3.85$.

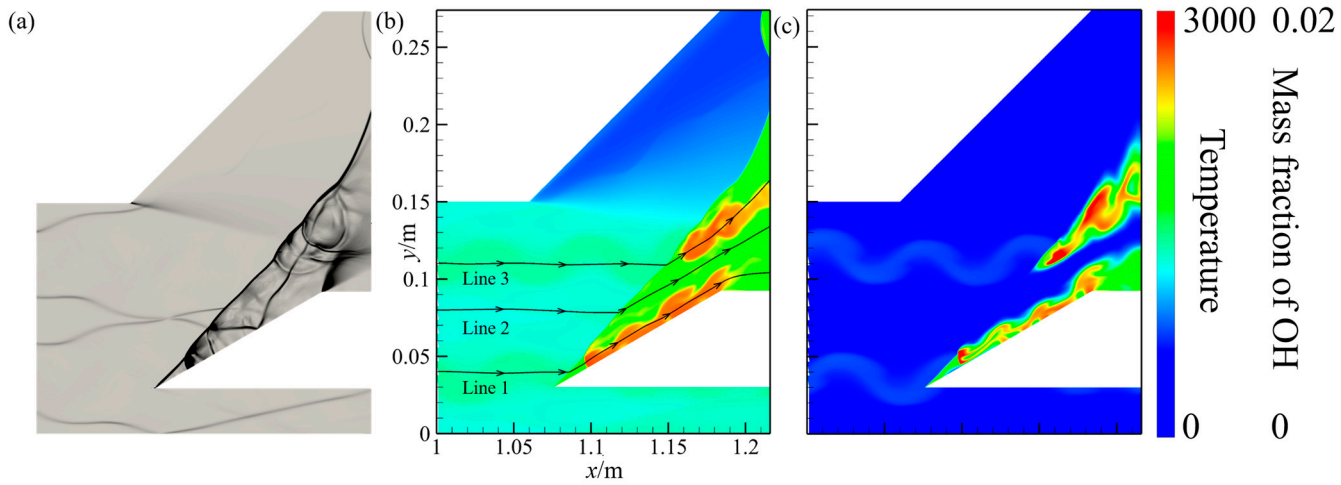

Figure 12. Oblique detonation induced by a 30° ramp. (**a**) Schlieren-like image of the combustor; (**b**) temperature distribution with schematic streamlines for three representative flow regions; (**c**) OH mass-fraction distribution.

The theoretical CJ parameters were then compared with the simulated parameters extracted from the main reacting region. The simulated values were extracted from the region immediately behind the leading coupled wave, where high temperature, high pressure, and an OH-rich reaction zone are observed. The simulated temperature, pressure, and local flow velocity in this region are 2979 K, 167 kPa, and 1629.93 m/s, respectively, which are higher than the corresponding theoretical CJ temperature, pressure, and detonation velocity. These results indicate that the coupled wave region involves strong compression and rapid heat release and that the local wave–reaction coupling strength is higher than that of the CJ reference state.

However, considering the non-uniform fuel distribution, confinement-induced shock interactions, and local flow stratification in the present combustor, the CJ-parameter comparison is not used here as an independent proof of overdriven detonation. Instead, it is used as auxiliary support together with the numerical schlieren image, pressure field, temperature field, and OH mass-fraction distribution. Specifically, the leading compression wave is spatially coupled with a rapid temperature rise and a thin OH-rich reaction zone immediately behind it. Based on these combined features, the stabilized wave system is interpreted as a strongly coupled wave–reaction structure with oblique-detonation-like characteristics under the present numerical framework, and it may exhibit local overdriven features.

Combining Figure 12a,c, it can be seen that the coupled reaction–wave system exhibits pronounced lateral stratification under the non-premixed inflow. The oblique detonation is primarily established in the upper combustor and stabilizes above the ramp after the flow traverses the jet-induced shear layer. This stabilized configuration indicates that inlet lateral non-uniformities in fuel distribution and thermodynamic state can markedly modulate the wave-front location and strength. As a result, reactive, non-reactive, and weakly reactive layers coexist in the combustor. Therefore, the oblique detonation in the 30° case does not form a continuous smooth front over the entire channel height, but exhibits a stabilized saltation-type ODW structure with pronounced spatial stratification. Here, line 1 represents a near-wall trajectory, line 2 a core-flow trajectory, and line 3 a shear-layer trajectory. These differences are reflected in the pressure and OH profiles in Figure 13. Pressure responds primarily to wave compression and subsequent recompression, whereas OH—an indicator of high-temperature exothermic chemistry—delineates the main reaction zone through its rise and peak locations relative to the oblique-detonation front.

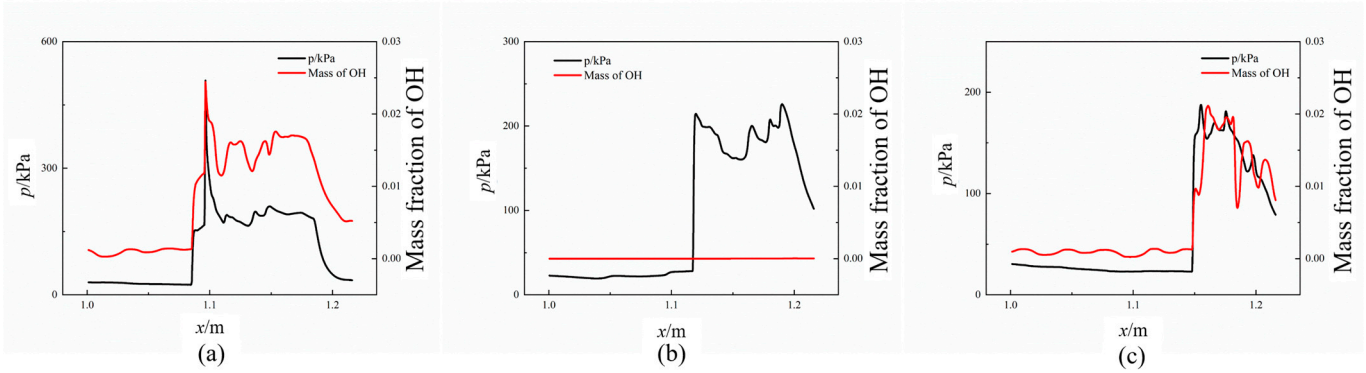

Figure 13. Pressure and OH radical profiles along representative trajectories in different flow regions: (**a**) Line 1; (**b**) Line 2; (**c**) Line 3.

As shown in Figure 13, although all three trajectories experience the same global wave system, their pressure evolutions and OH responses differ markedly. Along line 1, a pronounced plateau followed by a secondary pressure rise appears downstream of the primary compression, whereas the OH rise is not necessarily synchronous with the secondary pressure rise. Along line 2, a secondary pressure rise is also observed; however, the OH signal is substantially weaker than that along line 3. In contrast, along line 3, the OH rise closely follows the key segments of the pressure evolution, indicating stronger reaction–flow coupling. To determine whether the secondary pressure rise is dominated by heat release or recompression, we perform the following quantitative analysis.

First, to objectively identify the recompression region, the streamwise pressure gradient along each streamline is evaluated using a finite-difference approximation. The recompression region is then defined as the second continuous interval of positive pressure gradient that appears downstream of the primary compression peak, i.e., the continuous segment of $dp/dx > 0$ occurring after the pressure plateau. No additional artificial filtering was applied; however, the streamline-sampling procedure provides a spatial reconstruction of the pressure variation along the flow path and reduces the influence of noise to some extent. Based on this criterion, the recompression regions are identified as $x = [1.13108, 1.13715]$ for line 1, $x = [1.1565, 1.16556]$ for line 2, and $x = [1.15166, 1.15516]$ for line 3. The pressure rise across the recompression region is denoted as $\Delta p_{rc} = p(x_2) - p(x_1)$, and the corresponding normalized pressure rise is defined as $\Delta p_{rc^*} = \Delta p_{rc}/p(x_1)$. The results are summarized in Table 5.

Table 5. Parameters characterizing the contribution of the recompression region to the secondary pressure rise in different flow regions.

Line	$[x_1, x_2]$	Δp_{rc}/kPa	Δp_{rc^*}
1	[1.13108, 1.13715]	33.45	20.43%
2	[1.1565, 1.16556]	39.87	27.98%
3	[1.15166, 1.15516]	27.98	17.54%

Table 5 shows that a secondary pressure rise occurs along all three trajectories, but its origin is not necessarily the same. The secondary pressure rise may be driven by exothermic heat release (thermally driven expansion and associated wave modulation) or dominated by wave superposition and near-wall recompression.

To assess whether the secondary pressure rise is directly driven by heat release, we introduce a quantitative diagnostic based on the heat-release rate, Q. As illustrated in Figure 13, OH indicates the location of the main reaction zone. The recompression center x_{rc} is defined as the location of the maximum Q within the recompression region, whereas

the primary heat-release peak $x_{Q,\,peak}$ is defined as the global maximum of Q. The offset distance is defined as $\triangle x = \left| x_{rc} - x_{Q,\,peak} \right|$, and its nondimensional form is defined as $\Delta x^* = \Delta x / \mathrm{H}$, where H is the channel height. To separate the recompression and chemical heat-release contributions to the secondary pressure rise, the pressure-gradient criterion is first used to locate the secondary pressure-rise region. The streamwise locations of the pressure peak and the heat-release-rate peak within this region are then compared. If the pressure peak is clearly separated from the heat-release-rate peak, the pressure rise is mainly attributed to aerodynamic recompression induced by shock interaction or confinement effects. If the two peaks are nearly collocated, the pressure rise is considered to be dominated by chemical heat release. The results are summarized in Table 6.

Table 6. Offset distance between the recompression center and the primary heat-release peak, and the corresponding nondimensional values.

Line	Δx/m	Δx*
1	0.03874	0.258
2	0.04404	0.294
3	0.00438	0.029

The results indicate that for lines 1 and 2, the secondary pressure-rise region is not collocated with the primary heat-release peak, whereas line 3 shows clear collocation.

To further exclude the possible uncertainty associated with a single sampling time window, the same analysis was conducted for the previous sampling time ($t - 1$). The results show that the Δx^* is 0.179 for line 1 and 0.037 for line 3. These results are consistent with the conclusion obtained at time (t), indicating that the present attribution of the secondary pressure rise shows good repeatability over different sampling time windows.

To reduce ambiguity associated with using peak locations alone, we further evaluate the heat-release contribution within the recompression region, $R_{Q,rc} = \int_{x_1}^{x_2} Q dx / \int Q dx$. The results yield $R_{Q,rc}$ = 1.6%, 0.028% and 5.59% for lines 1–3, respectively. Together with the OH response in Figure 13, these two metrics lead to consistent conclusions. For lines 1 and 2, the secondary pressure rise is non-collocated with the intense reaction zone, and the heat-release contribution within the recompression region is negligible, indicating recompression-dominated behavior. In contrast, line 3 exhibits strong collocation with the main reaction zone and a larger $R_{Q,rc}$, characteristic of heat-release-dominated coupling.

The mass-averaged static and total pressures were further evaluated at the combustor inlet and outlet. For the present two-dimensional calculation, the mass-averaged pressure at a selected station was calculated using the line-integrated mass flux as the weighting factor:

$$\overline{p}_m = \frac{\int_L \rho u_n p \mathrm{d}L}{\int_L \rho u_n \mathrm{d}L} \tag{19}$$

where L is the selected inlet or outlet sampling line, and u_n is the velocity component normal to the sampling line. The same mass-weighting procedure was also used for the total pressure.

Based on the stabilized flow field, the mass-averaged static pressure increases from 25.532 kPa at the combustor inlet to 66.050 kPa at the combustor outlet, corresponding to an outlet-to-inlet static-pressure ratio of 2.587. However, the mass-averaged total pressure decreases from 2830.021 kPa to 993.244 kPa, giving a total-pressure recovery coefficient of 0.351. These results indicate that, although a clear combustor-level static-pressure rise is obtained after oblique-detonation initiation, a significant total-pressure loss still occurs in the constrained combustor.

The total-pressure loss is mainly associated with shock compression, shock reflection and interaction, viscous dissipation, mixing loss, and confinement effects. Since the present computational domain does not include a downstream nozzle, the overall pressure gain and thrust performance of a complete ODE system still require further evaluation, including the nozzle expansion process. Therefore, the mass-averaged pressure results reported here are extracted from the stabilized flow field and are mainly used to characterize the pressure variation within the combustor; they should not be directly interpreted as the complete engine-level pressure-gain performance.

3.3. Effects of Ramp Angle on Oblique-Detonation Initiation and Stabilization in a Constrained Supersonic Channel

After characterizing injection and mixing in the mixing section, we examine the effect of ramp angle on oblique-detonation initiation and stabilization. To maintain identical inflow and injection conditions across cases, the injection angle is fixed at 30° and the ramp angle is varied as 25°, 30°, and 35°. Figures 14–17 present contours of temperature, pressure, and H_2O/OH fields, and together with the time-resolved temperature snapshots in Figure 18, they illustrate the evolution from a non-initiated state to detonation onset and subsequent stabilization. The detonation morphology depends strongly on ramp angle: no self-sustained ODW is obtained for the 25° ramp; the stabilized ODW exhibits a saltation-type (discontinuous) front topology for the 30° ramp, whereas a smooth (continuous) front topology is obtained for the 35° ramp.

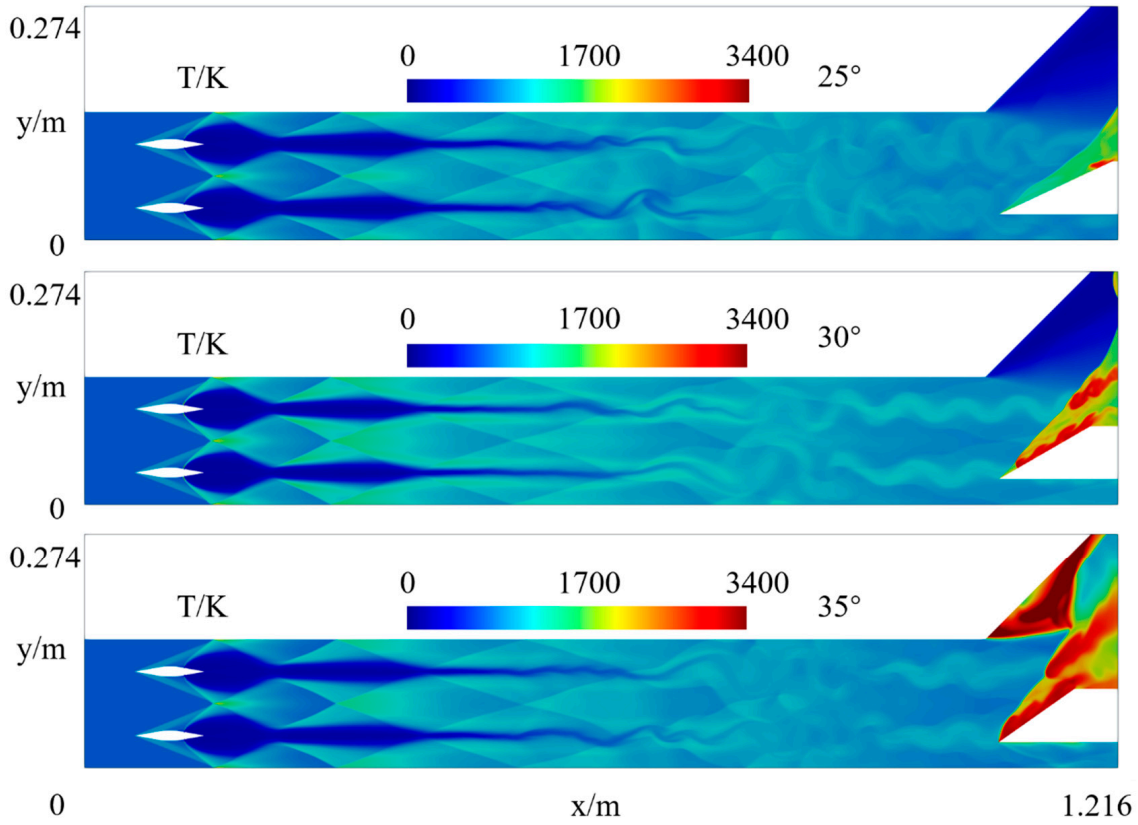

Figure 14. Temperature contours of the oblique-detonation flow field for three ramp angles.

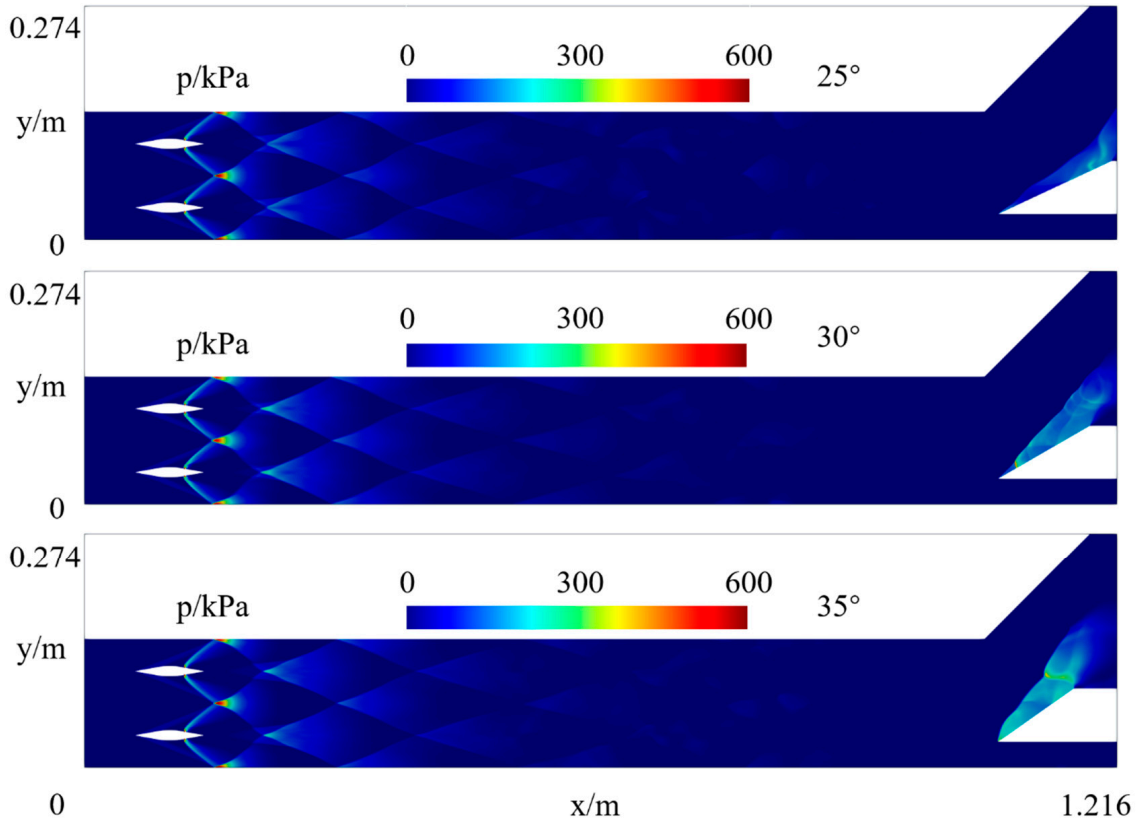

Figure 15. Pressure contours of the oblique-detonation flow field for three ramp angles.

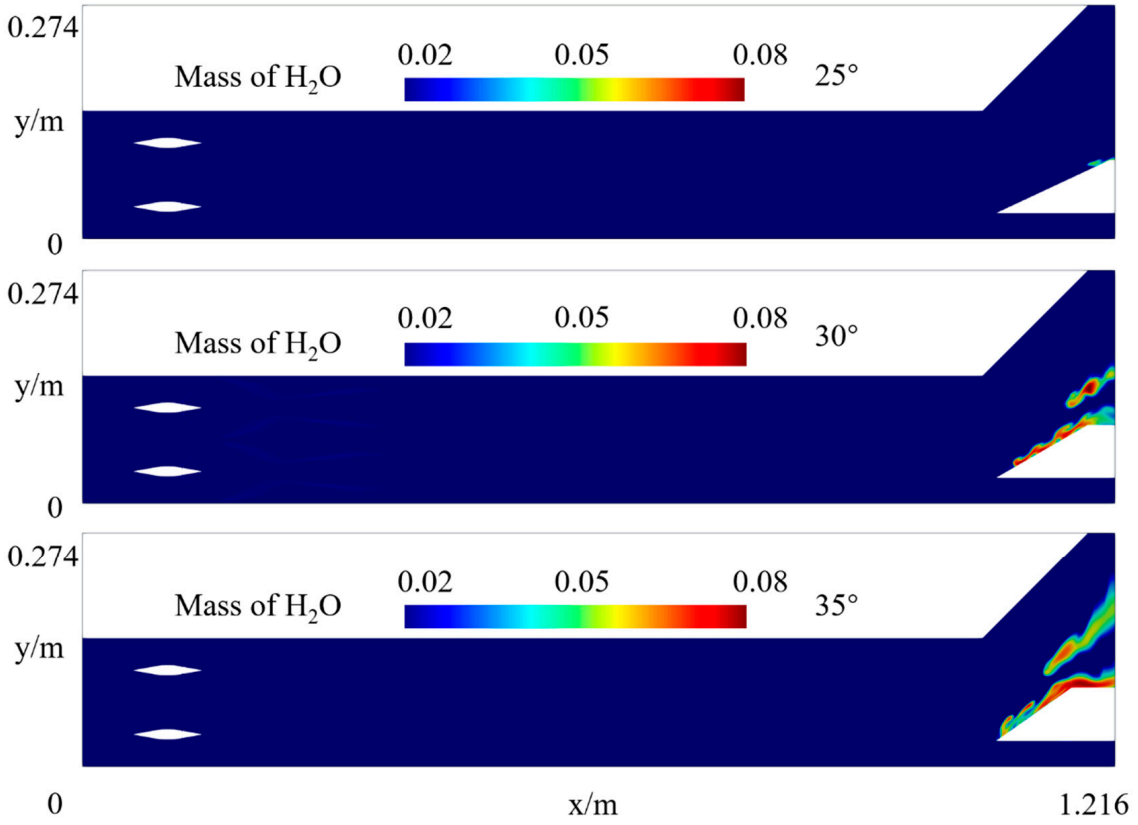

Figure 16. H_2O distribution contours for three ramp angles.

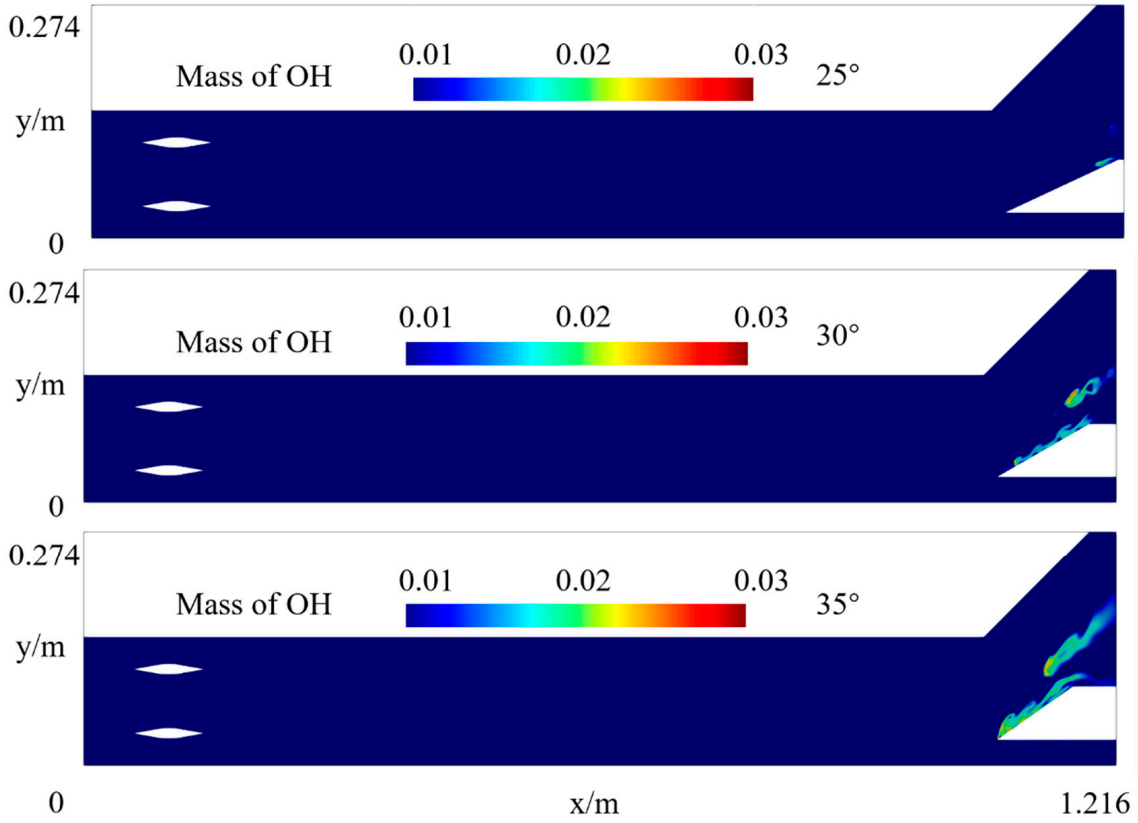

Figure 17. OH distribution contours for three ramp angles.

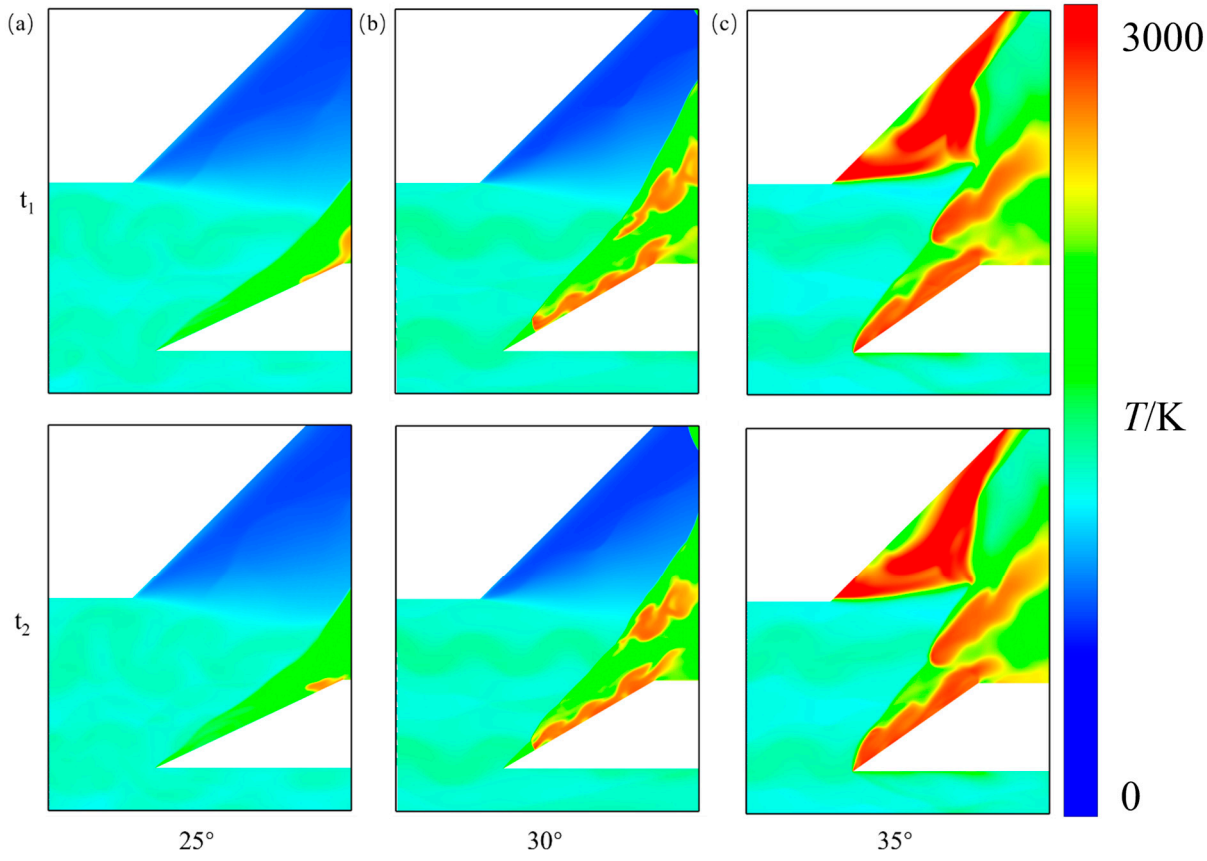

Figure 18. Temperature fields of the oblique detonation at different times: (**a**) 25° wedge angle; (**b**) 30° wedge angle; (**c**) 35° wedge angle.

Under the present non-uniform inflow, varying the ramp angle essentially modulates the compression strength of the oblique shock, thereby altering the spatial coupling among temperature, pressure, and chemical reactions. For the 25° ramp, the oblique-shock compression is comparatively weak. The flow-field response is dominated by aerodynamic compression heating and wave-system modulation, and a continuous, stable coupled structure of "high temperature–high pressure–high radical activity–product accumulation" cannot be established near the ramp. In the contours, this corresponds to limited enhancement of temperature and pressure, and the absence of a continuous band of OH and H_2O aligned with the wave front. Accordingly, no stabilized ODW is obtained for the 25° ramp under the present conditions.

When the ramp angle is increased to 30°, the enhanced oblique-shock compression elevates the post-shock temperature and pressure, substantially shortening the induction process. The OH field develops a distinct reactive layer near the strongly compressed region, while H_2O exhibits pronounced product accumulation farther downstream. The OH/H_2O distributions become increasingly co-located with high-temperature/high-pressure regions, indicating that the coupled sequence of compressive heating, rapid heat release, and wave-system strengthening approaches a stabilized state.

To ensure consistent quantitative comparisons across cases and to reduce the sensitivity of extrema to the strong unsteady fluctuations associated with transverse-wave bands (near triple points), peak quantities are extracted only from the non-transverse-wave region of the combustor ODW. Transverse-wave bands are identified using an objective thresholding procedure applied to the schlieren indicator $|\triangle p|$: connected regions exceeding the 95th percentile of the instantaneous field are classified as transverse-wave bands, and peak values of p_{max}, $T_{\max}$, and related quantities are evaluated outside these regions. With this procedure, the 30° ramp case yields a peak pressure of 277.23 kPa, a peak temperature of 3013 K, and a maximum H_2O mass fraction of 0.0765 within the non–transverse-wave region. These values are consistent with the coherent alignment of the high-p/high-T zones, reactive radical layer, and product-accumulation band along the primary wave front observed in Figures 14–17.

To exclude the influence of the selected threshold on the peak extraction, additional sensitivity tests were performed using the 90th- and 98th-percentile thresholds. The results show that when the 90th percentile threshold is used, the extracted temperature and pressure peaks are 2916.07 K and 253.47 kPa, respectively, showing noticeable differences from those obtained with the 95th percentile threshold. This is mainly because the 90th percentile threshold corresponds to a larger excluded region, which may remove not only the transverse-wave bands but also part of the non-transverse-wave main-flow region. In contrast, when the 98th percentile threshold is used, the extracted temperature and pressure peaks are 3087 K and 279.47 kPa, respectively, which are close to those obtained with the 95th percentile threshold. Therefore, the 95th percentile threshold is considered appropriate because it can exclude most localized high-gradient regions associated with transverse waves and triple points, while avoiding excessive removal of effective flow-field regions caused by a lower threshold.

In addition, a strong precompression region exists during the transition from the mixing section to the combustor entrance, induced by geometric contraction and flow turning. This region is characterized by a marked pressure rise near the ramp leading edge, a concurrent temperature increase, and the formation of a high-temperature band. Such a "high-p/high-T precompression environment" further modifies the local Mach number and density of the mixture, which is favorable to rapid reactions for cases with ramp angles of 30° and above.

With a further increase to 35°, stronger flow turning amplifies temperature and pressure and facilitates formation of a more continuous coupled structure near the ramp. Accordingly, the OH and H_2O signals are stronger and extend over a wider region than in the 30° case. Peaks extracted from the non-transverse-wave region increase accordingly, p_{max} = 393.87 kPa and T_{max} = 3173.57 K, with a peak H_2O mass fraction of 0.0779, quantitatively reflecting the enhanced compression and promoted reactions associated with a larger ramp angle.

Since the 35° ramp case exhibits stronger shock compression, more pronounced separation, and recirculation near the ramp, the y^+ distribution along the relevant walls was further evaluated to verify the near-wall mesh resolution for this condition. The minimum, mean, and maximum y^+ values along the ramp wall are 0.35, 1.813, and 4.072, respectively. For the upper combustor wall, the corresponding values are 0.2276, 1.0572, and 2.4863, respectively. Overall, the mean y^+ values along the relevant walls remain close to unity, and the maximum values are below 5, indicating that the first-layer mesh height generally satisfies the low-y^+ near-wall treatment requirement of the k-ω SST model. This provides near-wall mesh-resolution support for the analysis of separation, recirculation, and near-wall flow features in the 35° case.

Overall, the failure of the 25° case and the successful stabilization of the 30° and 35° cases are mainly attributed to the ramp-angle-dependent compression strength. The 25° ramp cannot sufficiently shorten the chemical induction process to establish sustained wave–reaction coupling, whereas the stronger compression produced by the 30° and 35° ramps promotes local and more continuous coupling between the leading wave and the reaction zone, respectively.

Meanwhile, an anomalous high-temperature zone above the ramp is observed without a corresponding increase in OH or H_2O, and the pressure there is relatively low, indicating that this feature is not attributable to localized exothermic chemistry or product recirculation. As suggested by the streamline pattern in Figure 19, it originates from boundary-layer separation and a separation-induced recirculation zone under stronger flow deflection. Within the recirculation zone, the flow velocity and density are reduced; after undergoing expansion and depressurization, a low-pressure core is formed. Concurrently, viscous dissipation and stagnation heat accumulation in the low-speed region lead to an anomalous rise in static temperature, producing the "high-temperature/low-pressure with negligible product formation" signature in the contours.

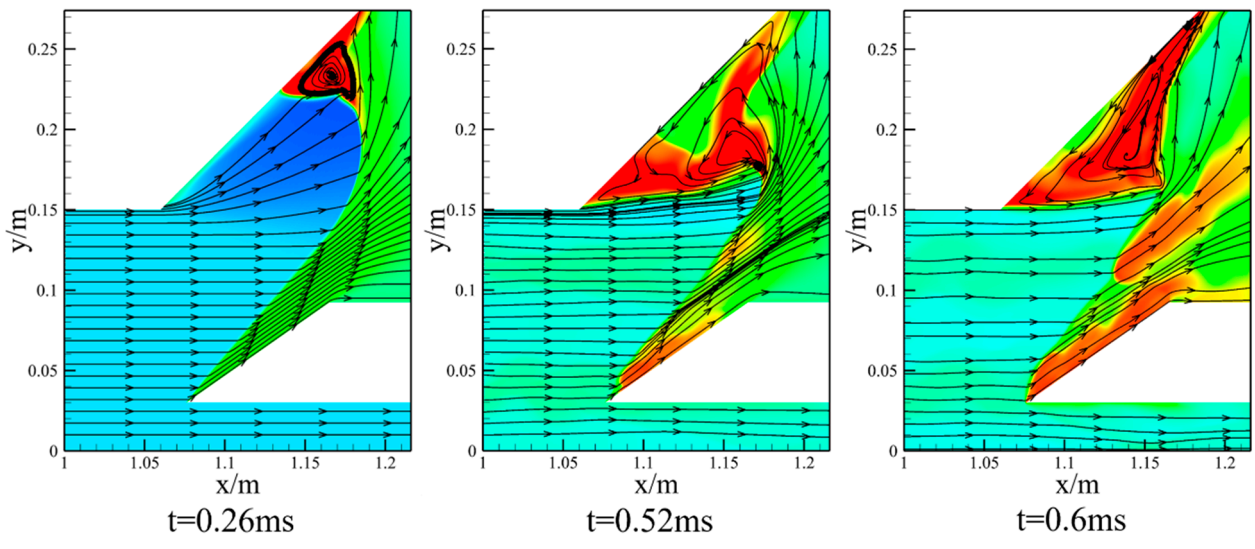

Figure 19. Schematic streamlines in the combustor for the 35° ramp case.

The experimental system and diagnostic method have been described in Section 2.4. Here, the high-speed imaging results are compared with the numerical schlieren images to assess whether the simulations reproduce the ramp-angle-dependent initiation trend, global wave topology, and stabilized-front morphology. It should be noted that the present experimental results are used mainly for qualitative validation of the global wave structure and ramp-angle-dependent initiation trend, rather than pointwise quantitative validation of the pressure, temperature, or heat-release fields.

Figure 20 presents a qualitative comparison between the numerical schlieren images and the experimental high-speed imaging results for the three ramp angles. For the 25° case, the flow is dominated by compression waves/shocks and only a weak reactive zone is observed, consistent with the prediction that compression is insufficient to form a continuous coupled reaction layer. For the 30° and 35° cases, initiation is achieved, and a distinct ODW front becomes stabilized and anchored over the ramp. The numerical schlieren images and high-speed imaging results show qualitative consistency in the ramp-angle-dependent initiation trend and global wave topology: the 30° case exhibits a saltation-type front topology, whereas the 35° case shows a smooth topology enabled by stronger compression and more complete post-front heat release.

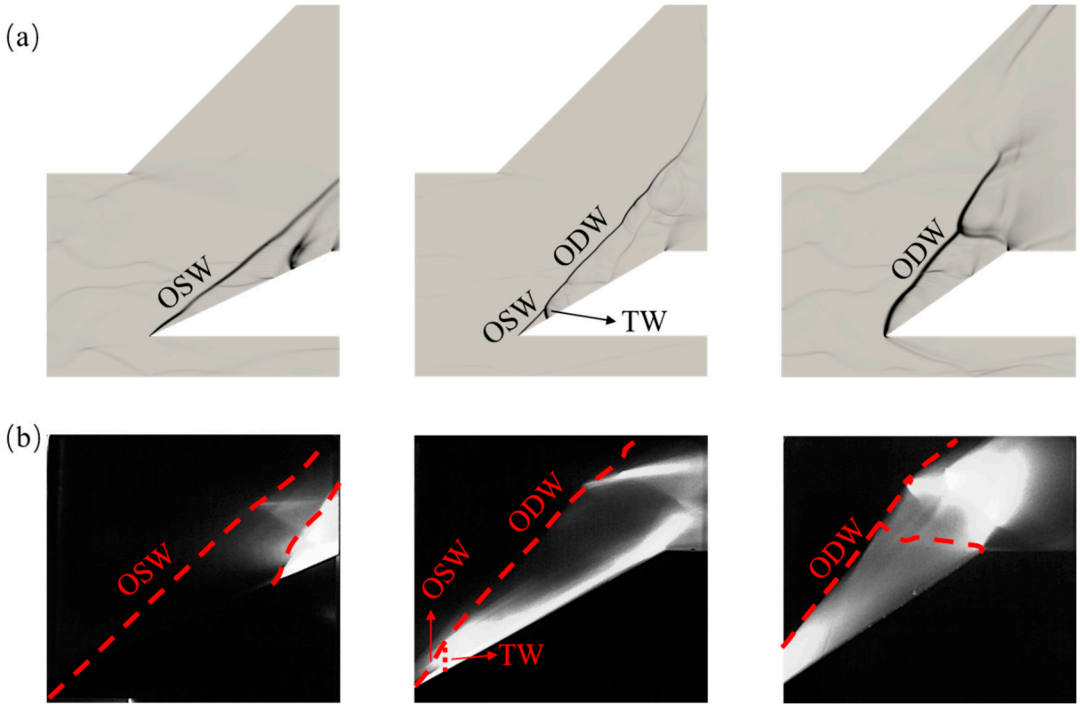

Figure 20. Comparison of numerical schlieren and high-speed imaging results for different ramp angles: (**a**) Numerical schlieren images for different ramp angles; (**b**) High-speed imaging results for different ramp angles.

As shown in Figure 21, further time-domain analysis of the high-speed image sequence indicates that, after initiation and establishment, the main oblique-detonation front exhibits only minor temporal variations in both position and overall morphology. No pronounced upstream/downstream drifting or structural degradation is observed, suggesting that the wave system can remain quasi-steady and stabilized over the ramp. This stabilized behavior is consistent with the numerically predicted stabilization location and wave-system topology, providing qualitative support for the predicted initiation threshold and morphology transition.

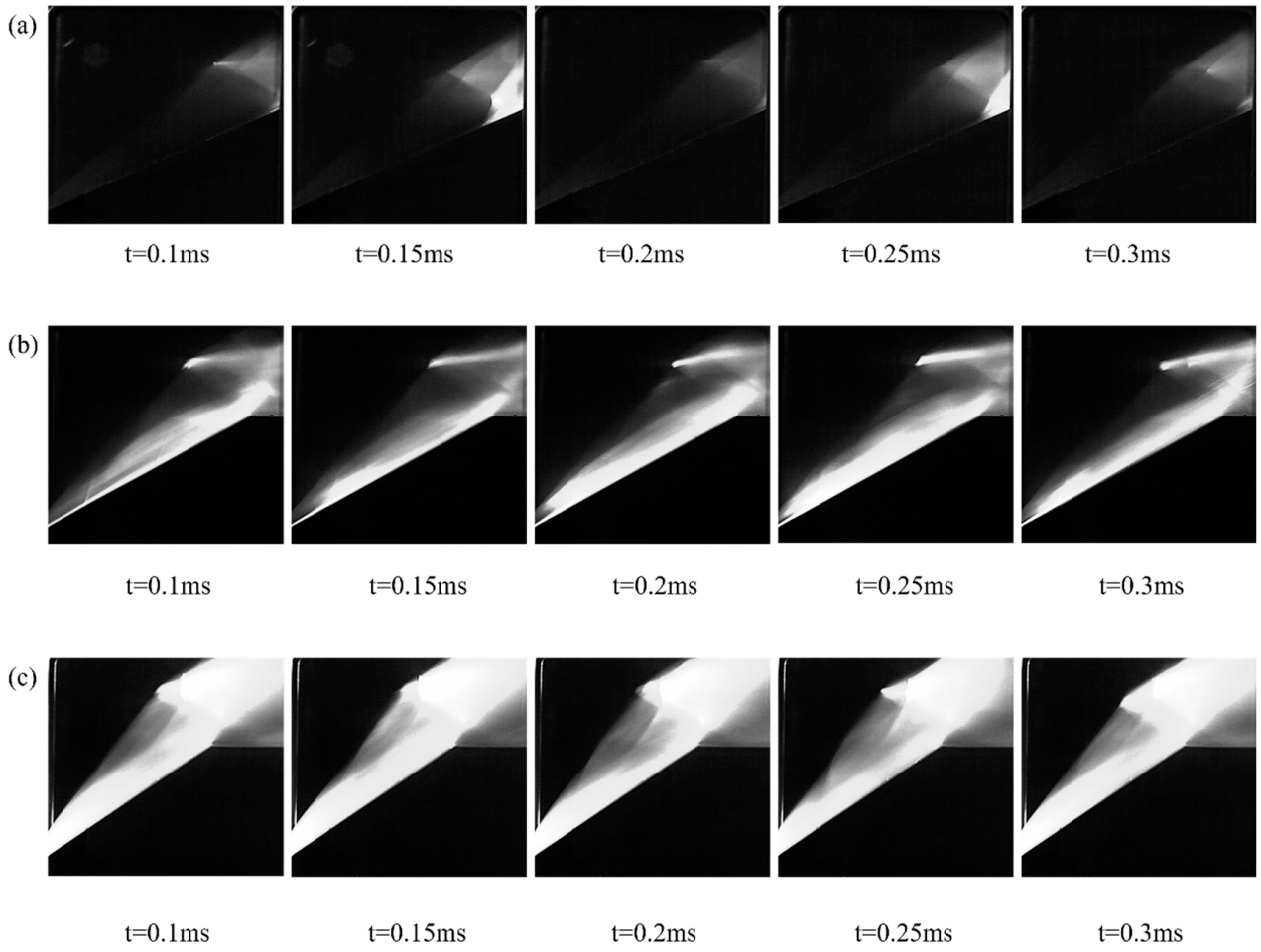

Figure 21. Time evolution of the wave-system structure at different instants: (**a**) High-speed images for the 25° ramp case; (**b**) High-speed images for the 30° ramp case; (**c**) High-speed images for the 35° ramp case.

In summary, the experimental observations and numerical results show qualitative consistency in the initiation threshold, stabilized front location, and overall wave-system topology, providing a basis for the subsequent mechanism-oriented analysis and for the design and optimization of combustor configurations with different ramp angles [13,14].

The present ramp-angle-dependent results further support the conclusion of Sun et al. that the evolution and stabilization of ODW structures are highly sensitive to wedge-angle variation [50]. In the present non-premixed constrained channel, the 25° ramp provides insufficient post-shock compression to establish self-sustained shock–reaction coupling, whereas the 30° and 35° ramps promote stabilized ODW formation. This trend also agrees with the findings of Vashishtha et al., who showed that reducing the effective induction length can promote the transition from an oblique shock wave to an oblique detonation wave [51].

Compared with the above studies, the present work further extends the discussion to a strongly stratified RP-3-surrogate inflow generated by transverse injection. However, since RP-3 is simplified as a gas-phase $C_{10}H_{22}$ surrogate in the present simulations, atomization, droplet evaporation, and two-phase spray–shock interactions are not included in the current model. Therefore, compared with realistic liquid RP-3 injection conditions, the present model still has certain limitations.

4. Conclusions

Using an RP-3 aviation-kerosene surrogate fuel $C_{10}H_{22}$, this study numerically investigates the initiation and stabilized structure of oblique detonation waves (ODWs) in a constrained supersonic channel under non-premixed transverse injection and ramp-induced compression. Simulations are performed for a Mach 8 inflow representative of a 30 km altitude flight condition with a fixed injection angle of 30°, and the predicted trends are qualitatively assessed against ground-based direct-connect hot-fire experiments. The main conclusions are as follows:

1. For the limited available mixing length, jet–crossflow interaction produces a strongly stratified, non-premixed inflow at the combustor entrance, with coexisting fuel-rich and fuel-lean regions and markedly non-uniform thermodynamic fields. The total-pressure recovery factor along the mixing section decreases downstream and asymptotically approaches ~0.49, providing an inlet-loss baseline for evaluating ODW initiation and stabilization.
2. A quantitative framework is proposed to interpret the pressure-gain mechanism based on identification of the recompression region and assessment of heat-release co-location. The recompression zone is determined using a pressure-gradient criterion, and the secondary pressure-rise mechanism is classified as recompression-dominated or heat-release-dominated using metrics $\Delta x/H$ and $R_{Q,rc}$. For the 30° ramp case, pronounced spatial misalignment and a low heat-release contribution are observed along the near-wall and core trajectories, indicating a recompression-dominated secondary pressure rise. In contrast, the shear-layer trajectory exhibits smaller misalignment and a higher heat-release contribution, consistent with heat-release-dominated coupling.
3. By altering the compression strength, the ramp angle governs the initiation window and stabilized wave topology and further modulates near-wall separation/recirculation and the spatial distribution of the reaction zone. Under the present injection and inflow conditions, no stabilized ODW is obtained for the 25° ramp, whereas stabilized ODWs are obtained for both the 30° and 35° ramps. Increasing the ramp angle from 30° to 35° transitions the stabilized wave-front from a saltation-type topology to a smooth topology, accompanied by an increase in primary-front peak values when evaluated outside transverse-wave bands/triple-point regions. In addition, the 35° case exhibits localized separation-induced recirculation characterized by high temperature and low pressure with comparatively weak product formation and heat release, indicating redistribution of reaction due to boundary-layer dynamics. High-speed imaging and numerical schlieren show qualitative consistency in initiation threshold, stabilization location, and topology transition, supporting the predictive capability of the present model for constrained-channel ODW structures.

Author Contributions: Z.W.: Visualization; Writing—original draft; Writing—review and editing; B.L.: Methodology; Supervision; Writing—review and editing; K.W.: Writing—review and editing; R.W.: Formal analysis; C.W.: Validation; S.H.: Formal analysis. All authors have read and agreed to the published version of the manuscript.

Funding: This research received no external funding.

Data Availability Statement: The data presented in this study are available on request from the corresponding author.

Acknowledgments: The authors would like to thank Xi'an Modern Chemistry Research Institute.

Conflicts of Interest: The authors declare no conflicts of interest.

Abbreviations

The following abbreviations are used in this manuscript:

RP-3	A specific type of aviation kerosene
ODW	Oblique Detonation Wave
ODE	Oblique Detonation Engine
CFD	Computational Fluid Dynamics
RANS	Reynolds-averaged Navier–Stokes
SST	Shear Stress Transport
PaSR	Partially Stirred Reactor
NASA	National Aeronautics and Space Administration
CFL	Courant–Friedrichs–Lewy number
TPRC	Total-Pressure Recovery Coefficient
OSW	Oblique Shock Wave
TW	Transverse Wave

References

1. Heiser, W.H.; Pratt, D.T. *Hypersonic Airbreathing Propulsion*; AIAA: Reston, VA, USA, 1994.
2. Drummond, J.; Diskin, G.; Cutler, A. Fuel-Air Mixing and Combustion in Scramjets. In *Proceedings of the 38th AIAA/ASME/SAE/ASEE Joint Propulsion Conference and Exhibit*; AIAA: Reston, VA, USA, 2002.
3. Curran, E.T. Scramjet Engines: The First Forty Years. *J. Propuls. Power* **2001**, *17*, 1138–1148. [CrossRef]
4. Zhao, D. Ramjets/scramjets aerodynamics: A progress review. *Prog. Aerosp. Sci.* **2023**, *143*, 100958. [CrossRef]
5. Fry, R.S. A Century of Ramjet Propulsion Technology Evolution. *J. Propuls. Power* **2004**, *20*, 27–58. [CrossRef]
6. Gutmark, E.J. Pressure gain combustion. *Shock Waves* **2021**, *31*, 619–621. [CrossRef]
7. Wolański, P. Detonative propulsion. *Proc. Combust. Inst.* **2013**, *34*, 125–158. [CrossRef]
8. Teng, H.H.; Jiang, Z.L. On the transition pattern of the oblique detonation structure. *J. Fluid Mech.* **2012**, *713*, 659–669. [CrossRef]
9. Yang, P.; Ng, H.D.; Teng, H. Numerical study of wedge-induced oblique detonations in unsteady flow. *J. Fluid Mech.* **2019**, *876*, 264–287. [CrossRef]
10. Li, R.; Xu, J.; Lv, H. Decoupled and coupled nozzle performance of the oblique detonation wave engine in the level flight states. *Int. J. Hydrogen Energy* **2025**, *99*, 939–955. [CrossRef]
11. Sun, J.; Yang, P.; Tian, B.; Chen, Z. Evolution and Control of Oblique Detonation Wave Structure in Unsteady Inflow. *AIAA J.* **2023**, *61*, 4808–4820. [CrossRef]
12. Qin, Q.; Li, L.; Han, F.; Yao, Q.; Liu, Y.; Yuan, M.; Li, X.; Ji, T.; Li, J. Expansion wave-reinforced initiation of the oblique detonation wave. *Phys. Fluids* **2024**, *36*, 086116. [CrossRef]
13. Teng, H.; Ng, H.D.; Jiang, Z. Initiation characteristics of wedge-induced oblique detonation waves in a stoichiometric hydrogen-air mixture. *Proc. Combust. Inst.* **2017**, *36*, 2735–2742.
14. Teng, H.; Tian, C.; Zhang, Y.; Zhou, L.; Ng, H.D. Morphology of oblique detonation waves in a stoichiometric hydrogen–air mixture. *J. Fluid Mech.* **2021**, *913*, A1. [CrossRef]
15. Rosato, D.A.; Thornton, M.; Sosa, J.; Bachman, C.; Goodwin, G.B.; Ahmed, K.A. Stabilized detonation for hypersonic propulsion. *Proc. Natl. Acad. Sci. USA* **2021**, *118*, e2102244118.
16. Han, X.; Zhang, W.S.; Zhang, Z.J.; Yuan, C.; Han, G.; Liu, Y. Experimental study on RP3 aviation kerosene oblique detonation engine. *J. Exp. Fluid Mech.* **2024**, *38*, 21–29. [CrossRef]
17. Zhang, Z.; Liu, Y.; Wen, C. Mechanisms of the destabilized Mach reflection of inviscid oblique detonation waves before an expansion corner. *J. Fluid Mech.* **2022**, *940*, A29. [CrossRef]
18. Xiang, G.; Zhang, Y.; Gao, X.; Li, H.; Huang, X. Oblique detonation waves induced by two symmetrical wedges in hydrogen-air mixtures. *Fuel* **2021**, *295*, 120615. [CrossRef]
19. Qin, J.; Zhu, D. Criticality for Oblique Detonation Waves Induced by a Finite Wedge in a Hydrogen–Air Mixture. *Aerospace* **2023**, *10*, 508. [CrossRef]
20. Yao, J.; Lin, Z. Numerical investigation of jet-wedge combinatorial initiation for oblique detonation wave in supersonic premixed mixture. *Phys. Fluids* **2023**, *35*, 026101. [CrossRef]
21. Teng, H.; Ng, H.D.; Li, K.; Luo, C.; Jiang, Z. Evolution of cellular structures on oblique detonation surfaces. *Combust. Flame* **2015**, *162*, 470–477. [CrossRef]

22. Yang, P.; Teng, H.; Jiang, Z.; Ng, H.D. Effects of inflow Mach number on oblique detonation initiation with a two-step induction-reaction kinetic model. *Combust. Flame* **2018**, *193*, 246–256. [CrossRef]
23. Guo, H.; Yang, H.; Zhao, N.; Li, S.; Zheng, H. Influence of incoming flow velocity and mixture equivalence ratio on oblique detonation characteristics. *Aerosp. Sci. Technol.* **2021**, *119*, 107088. [CrossRef]
24. Liu, Y.; Wang, H.; Mével, R.; Luo, K.; Fan, J. Numerical study of wedge-induced oblique detonation waves in homogeneous and inhomogeneous n-dodecane/air mixtures. *Phys. Fluids* **2025**, *37*, 066118. [CrossRef]
25. Han, X.; Liu, Y.; Zhang, Z.; Zhang, W.; Yuan, C.; Han, G.; Jiang, Z. Experimental demonstration of forced initiation of kerosene oblique detonation by an on-wedge trip in an ODE model. *Combust. Flame* **2023**, *258*, 113102. [CrossRef]
26. Iwata, K.; Hanyu, N.; Maeda, S.; Obara, T. Experiments on critical behavior of oblique detonation wave in stratified mixtures. *Phys. Fluids* **2024**, *36*, 096113. [CrossRef]
27. Du, P.; Xue, R.; Wu, Y.; Liu, J. Study on the flow field of a kerosene-fueled integrated inlet-combustor-nozzle oblique detonation engine. *Phys. Fluids* **2023**, *35*, 066127.
28. Han, X.; Qiu, R.; You, Y. Flow characteristics and propulsive performance of oblique detonation waves induced by a transverse jet. *Phys. Fluids* **2024**, *36*, 076133. [CrossRef]
29. Sun, S.; Liu, Y.; Xiang, G. Effects of kerosene pre-injection and geometric parameters on oblique detonation initiation and stabilization in a combustor. *Phys. Fluids* **2025**, *37*, 046130. [CrossRef]
30. Sun, Y.; Wang, S.; Zhao, M.; Guo, H. Influence of inhomogeneous distribution of inflow equivalence ratio on oblique detonation morphology and characteristic. *Phys. Fluids* **2024**, *36*, 076104. [CrossRef]
31. Sun, J.; Yang, P.; Chen, Z. Dynamic interaction patterns of oblique detonation waves with boundary layers in hypersonic reactive flows. *Combust. Flame* **2025**, *271*, 113832. [CrossRef]
32. Ramachandran, S.; Yang, S. Micro-jetting and Transverse Waves in Oblique Detonations. *Combust. Flame* **2024**, *265*, 113506. [CrossRef]
33. Tang, Z.; Liu, X.; Hu, C.; Xue, R.; Wang, J. Numerical study on flow field characteristics and performance of a Mach 10 internal injection kerosene-fueled oblique detonation engine. *Phys. Fluids* **2024**, *36*, 106142. [CrossRef]
34. Shang, J.; Hu, G.; Wang, Q.; Xiang, G.; Zhao, W. Progress of Experimental Studies on Oblique Detonation Waves Induced by Hyper-Velocity Projectiles. *Aerospace* **2024**, *11*, 715. [CrossRef]
35. Kurganov, A.; Noelle, S.; Petrova, G. Semidiscrete Central-Upwind Schemes for Hyperbolic Conservation Laws and Hamilton--Jacobi Equations. *SIAM J. Sci. Comput.* **2006**, *23*, 707–740. [CrossRef]
36. Mcgough, D. Detonation Modeling in OpenFOAM Using Adaptive Mesh Refinement. Master's Thesis, University of Colorado at Boulder, Boulder, CO, USA, 2020.
37. Project Webpage. Available online: https://Github.Com/duncanam/rhoReactingCentralFoam (accessed on 17 March 2025).
38. Péquin, A.; Iavarone, S.; Malpica Galassi, R.; Parente, A. The partially stirred reactor model for combustion closure in large eddy simulations: Physical principles, sub-models for the cell reacting fraction, and open challenges. *Phys. Fluids* **2022**, *34*, 055122. [CrossRef]
39. Hairer, E.; Wanner, G. *Solving Ordinary Differential Equations II: Stiff and Differential-Algebraic Problems*; Springer: Berlin/Heidelberg, Germany, 1996.
40. Menter, F.R. Two-equation eddy-viscosity turbulence models for engineering applications. *AIAA J.* **1994**, *32*, 1598–1605. [CrossRef]
41. Le, J.; Yang, S.; Liu, W.; Xing, J. Massively Parallel Simulations of Kerosene-Fueled Model Scramjet. In *Proceedings of the AIAA/CIRA 13th International Space Planes and Hypersonics Systems and Technologies Conference*; AIAA: Reston, VA, USA, 2005.
42. Du, P.; Xue, R.; Wang, C.; Zhang, Y.; Xu, C. Numerical simulation of oblique detonation engine performance based on kerosene fuel. *J. Aerosp. Power* **2023**, *38*, 2349–2359.
43. Chen, B.H.; Liu, J.Z.; Yao, F.; He, Y.; Yang, W.J. Ignition delay characteristics of RP-3 under ultra-low pressure (0.01–0.1 MPa). *Combust. Flame* **2019**, *210*, 126–133. [CrossRef]
44. Lehr, H.F. Experiments on shock-induced combustion. *Astronaut. Acta* **1972**, *17*, 589–597.
45. Yungster, S.; Eberhardt, S.; Bruckner, A.P. Numerical simulation of hypervelocity projectiles in detonable gases. *AIAA J.* **1991**, *29*, 187–199. [CrossRef]
46. Xin, Y.; Jiang, Z.; Guo, S.; Shen, L.; Xiang, G.; Wang, Q. Exploration of initiation and stabilization properties of oblique detonation in a combustor with hydrogen fuel pre-injection. *Int. J. Hydrogen Energy* **2024**, *91*, 584–595.
47. Wang, K.; Wu, Z.; Li, B.; Feng, X.; Shu, H.; Hu, S.; Lin, Z. Investigation of mixing and initiation characteristics of oblique detonation engine in confined spaces. *Case Stud. Therm. Eng.* **2026**, *81*, 108005. [CrossRef]
48. Danckwerts, P.V. The definition and measurement of some characteristics of mixtures. *Appl. Sci. Res. Sect. A* **1952**, *3*, 279–296. [CrossRef]
49. Jiang, L.Y. An alternative approach to evaluate fuel/air mixing quality. *Aeronaut. J.* **2021**, *125*, 1469–1483. [CrossRef]

50. Sun, J.; Yang, P.; Tian, B.; Chen, Z. Effects of wedge-angle change on the evolution of oblique detonation wave structure. *Phys. Fluids* **2022**, *34*, 096112. [CrossRef]
51. Vashishtha, A.; Panigrahy, S.; Campi, D.; Callaghan, D.; Nolan, C.; Deiterding, R. Oblique Detonation Wave Control with O_3 and H_2O_2 Sensitization in Hypersonic Flow. *Energies* **2022**, *15*, 4140. [CrossRef]